

# JGR Atmospheres

## RESEARCH ARTICLE

10.1029/2020JD032895

### Key Points:

- Modeled migrating semidiurnal tide (SW2) mimicks radar observations, albeit wind biases may weaken SW2 peak in wintertime
- Interactions between SW2 and quasi-stationary planetary waves (PWs) during SSWs may excite non-migrating semidiurnal tides
- SW2 interactions with slow westward PWs may excite semidiurnal-tide-like waves with near 12-h period, extracted for the first time in a model

### Correspondence to:

V. Limpasuvan,  
[var@coastal.edu](mailto:var@coastal.edu)

### Citation:

Zhang, J., Limpasuvan, V., Orsolini, Y. J., Espy, P. J., & Hibbins, R. E. (2021). Climatological westward-propagating semidiurnal tides and their composite response to sudden stratospheric warmings in SuperDARN and SD-WACCM-X. *Journal of Geophysical Research: Atmospheres*, 126, e2020JD032895. <https://doi.org/10.1029/2020JD032895>

Received 7 APR 2020

Accepted 23 DEC 2020

### Author Contributions:

**Conceptualization:** V. Limpasuvan, Y. J. Orsolini

**Writing – original draft:** J. Zhang, V. Limpasuvan, Y. J. Orsolini, P. J. Espy, R. E. Hibbins

**Writing – review & editing:** J. Zhang, V. Limpasuvan, Y. J. Orsolini, P. J. Espy, R. E. Hibbins

© 2021. The Authors.

This is an open access article under the terms of the Creative Commons Attribution-NonCommercial-NoDerivs License, which permits use and distribution in any medium, provided the original work is properly cited, the use is non-commercial and no modifications or adaptations are made.

# Climatological Westward-Propagating Semidiurnal Tides and Their Composite Response to Sudden Stratospheric Warmings in SuperDARN and SD-WACCM-X

J. Zhang<sup>1</sup>, V. Limpasuvan<sup>1</sup> , Y. J. Orsolini<sup>2,3</sup> , P. J. Espy<sup>3,4</sup> , and R. E. Hibbins<sup>3,4</sup> 

<sup>1</sup>Department of Marine Science, Coastal Carolina University, South Carolina, USA, <sup>2</sup>Norwegian Institute of Air Research, Kjeller, Norway, <sup>3</sup>Norwegian University of Science and Technology, Trondheim, Norway, <sup>4</sup>Birkeland Centre for Space Science, Bergen, Norway

**Abstract** Using the Super Dual Auroral Radar Network observations (clustered around 60°N) and NCAR CESM2.0 extended Whole Atmosphere Community Climate Model nudged with reanalyzes, we examine the climatology of semidiurnal tides in meridional wind associated with the migrating component (SW2) and non-migrating components of wavenumbers 1 (SW1) and 3 (SW3). We then illustrate their composite response to major sudden stratospheric warmings (SSWs). Peaking in late summer and winter, the climatological SW2 amplitude exceeds SW1 and SW3 except around late Fall and Spring. The winter climatological peak is absent in the model perhaps due to the zonal wind bias at the observed altitudes. The observed SW2 amplitude declines after SSW onset before enhancing ~10 days later, along with SW1 and SW3. Within the observed region, the simulated SW2 only amplifies after SSW onset, with minimal SW1 and SW3 responses. The model reveals a stronger SW2 response above the observed location, with diminished amplitude before and enhancement after SSW globally. This enhancement appears related to increased equatorial ozone heating and background wind symmetry. The strongest SW1 and SW3 growth occurs in the Southern Hemisphere before SSW. SW2 and quasi-stationary planetary wave activities are temporally collocated during SSW suggesting that their interactions excite SW1 and SW3. After SSW, the model also reveals (1) semidiurnal-tide-like perturbations generated possibly by the interactions between SW2 and westward-traveling disturbances and (2) the enhancement of migrating semidiurnal lunar tide in the Northern Hemisphere that exceeds non-migrating tidal and semidiurnal-tide-like responses. The simulated eastward-propagating semidiurnal tides are briefly examined.

## 1. Introduction

Atmospheric solar tides are planetary-scale oscillations generated predominantly by the 24-h periodic solar heating and its sub-harmonics of 12-, 8-, and 6-h periods. Heating occurs through solar energy absorption by atmospheric constituents like water vapor throughout the troposphere, ozone in the stratosphere, and molecular oxygen and nitrogen in the thermosphere (Forbes, 1984). Most dominant tidal variations travel westward synchronously with the Sun and are referred to as migrating tides. Globally, the migrating semidiurnal tide of zonal wavenumber 2 is the most dominant tidal feature at the 12-h period. Its generation is attributed to solar absorption by low-latitude stratospheric ozone (Chapman & Lindzen, 1970). Following the standard tidal nomenclature, we refer to this westward-propagating migrating semidiurnal tide as SW2.

Other atmospheric solar tides can be stationary or propagate eastward or westward relative to the apparent movement of the Sun. The origins of these non-migrating tides are not as obvious, as their forcing mechanisms and propagation characteristics can differ. They can arise from the latent heating associated with deep convection or the solar heating of longitudinally dependent atmospheric constituents such as water vapor or ozone (Forbes et al., 2003; Hagan & Forbes, 2003). Non-linear interactions between tides or between migrating tides and quasi-stationary planetary-scale waves (QSPWs) may likewise excite non-migrating tides (Forbes et al., 2003; Teitelbaum & Vial, 1991). During the solstice, westward-propagating non-migrating semidiurnal tides with zonal wavenumbers 1 and 3 (hereafter, SW1 and SW3, respectively) can be generated in the Northern Hemisphere winter stratosphere and mesosphere through the interactions between QSPW of zonal wavenumber 1 (hereafter, QSPW1) and SW2. The resultant SW1 and SW3 can propagate upward to the lower thermosphere (Angelats i Coll & Forbes, 2002; Miyoshi et al., 2017).

Collectively, SW1, SW2, and SW3 are the major components of the total (i.e., migrating and non-migrating) westward-propagating semidiurnal tide (Iimura et al., 2010). Their variations have been suggested to respond strongly to the major stratospheric sudden warming (SSW) phenomenon. Previous studies have documented the complex SW2 behavior through the SSW lifecycle, characterized initially by a decline around SSW onset when the zonal-mean zonal wind reverses. Then, at least for strong and persistent SSW events with an elevated stratopause, the SW2 amplitude increases, maximizing around two weeks after the SSW onset (Conte et al., 2019; Orsolini et al., 2017; Pedatella et al., 2014, 2012; Pedatella & Forbes, 2010; Pedatella & Liu, 2013; Sassi et al., 2013). With the enhanced QSPW1 activity typically associated with SSW onset, the SW1 and SW3 amplitudes can increase as SW2 interacts with QSPW1, as suggested by Angelats i Coll and Forbes (2002), Liu et al. (2010), and Pedatella and Forbes (2010) and modeled by Miyoshi et al. (2017). These anomalous semidiurnal tidal behaviors may arise through changes during SSWs in the low-latitude ozone distribution (Goncharenko et al., 2012; Limpasuvan et al., 2016; Siddiqui et al., 2019) or in the background zonal wind structure that forms the tidal waveguide (Jin et al., 2012).

In general, observing short-term variability of the semidiurnal tidal components is challenging. Asynoptic mapping, using the along-track profiles of polar-orbiting satellites, cannot resolve perturbations of periods smaller than 24 h (Salby et al., 1982). Instead, a two-dimensional Fourier fitting technique, with a long sliding temporal window, like that proposed by Forbes et al. (1997), has been employed to extract climatological semidiurnal tides (e.g., Truskowski et al. (2014) and references therein) and their variations during SSW events (e.g., Sridharan, 2019). Single-station observations can resolve the 12-h tidal signature but, independently, cannot distinguish zonal wavenumbers. Consequently, the extracted signal at a station constitutes the total semidiurnal tide (SDT) comprising of SW2 along with other non-migrating semidiurnal variations in the observational window. Nevertheless, various single stations have observed that the mid-to high-latitude SDT amplitude tends to decline as the stratospheric wind reverses during SSW before recovering to reach or exceed the previous amplitude value (e.g., Bhattacharya et al., 2004; Conte et al., 2019; Nozawa et al., 2012; Orsolini et al., 2017).

Recently, Hibbins et al. (2019) combined multiple, simultaneous single-station radar observations to separate longitudinal from temporal variations and to explicitly extract SW1, SW2, and SW3. Clustered around 60°N, these stations measure horizontal winds around 95 km as part of the Super Dual Auroral Radar Network (SuperDARN). Based on 13 SSW events, these authors reported a robust, composite SW2 amplitude reduction after SSW onset followed by an enhancement. Additionally, they identified a smaller accompanying increase in SW1 and SW3 amplitudes. However, the exact nature of the SW1 and SW3 enhancement during SSWs remains uncertain. Based on a network of five specular meteor radars (SMR) centered near 49°N, another recent study by He and Chau (2019) did not find noticeable SW1 and SW3 responses to SSWs. These authors suggested that what had been interpreted before as enhanced SW1 and SW3 may be non-tidal signatures with zonal wavenumbers 1 and 3 but with periods slightly higher or lower than 12 h (hereafter,  $\tilde{S}W1$  and  $\tilde{S}W3$ , respectively). These features may result from the resonance interaction between SW2 and traveling planetary-scale waves (PWs) of zonal wavenumber 1 with westward period in the range 10–20 days (hereafter, WPW1), as initially hypothesized by He et al. (2017). These WPW1s may be associated with the quasi 16-days wave (e.g., McDonald et al., 2011) or westward PWs present following an SSW onset (e.g., Limpasuvan et al., 2016). We refer to  $\tilde{S}W1$  and  $\tilde{S}W3$  as semidiurnal-tide-like waves.

Besides the response of solar tides, observations and model simulations both suggest the enhancement of the 12.42-h migrating semidiurnal lunar tide (M2) in the mesosphere and lower thermosphere (MLT) during SSW events (Chau et al., 2015; Forbes & Zhang, 2012; He & Chau, 2019; Lin et al., 2019; Pedatella et al., 2014). M2 arises from the gravitational potential between the Earth and the Moon (Chapman & Lindzen, 1970). With the M2 period close to SW2, observations of changes in the SW2 component during SSW could also contain the M2 signature.

In this paper, we examine both the climatological features of the semidiurnal tides (SW1, SW2, and SW3) and semidiurnal-tide-like waves ( $\tilde{S}W1$  and  $\tilde{S}W3$ ) in the MLT region as well as their mean response to SSWs. Along with SuperDARN observations, we use hourly simulations from the newly released Whole Atmosphere Community Climate Model with Thermosphere and Ionosphere Extension (WACCM-X) that is part of the National Center for Atmospheric Research (NCAR) Community Earth System Model (Danabasoglu et al., 2020) version 2.0 (CESM2.0). Previously, in Limpasuvan et al. (2016), we presented the composite

SW2 response to SSW based on the NCAR Whole Atmosphere Community Climate Model (WACCM; Marsh et al., 2013) with a model top near 130 km. However, uncertainty looms over the influence that the relatively low vertical boundary condition and the limited physical representation in the thermosphere may have on the tidal structure. Extended through the thermosphere (beyond ~500 km), WACCM-X can fully resolve the tidal vertical structure. In undergoing key changes in its numerical schemes and representation of physical processes, the new version of WACCM-X has improved simulations of tides and upper atmospheric variability due to lower atmospheric forcing (Liu et al., 2018). This is crucial since we are interested in SSWs which occur in the lower atmosphere, but their impact on tides can extend well into the thermosphere. While SuperDARN observes the MLT over a limited region (namely, near 60°N and around 95 km), the model allows us to not only compare tidal behaviors at the observed location but also to elucidate their global response.

To our knowledge, this paper is the first to report the robust behaviors of these phenomena using the unique combination of CESM2.0 WACCM-X and SuperDARN. Furthermore, for the first time in a model study, we examine the climatological behavior and response to SSW of semidiurnal-tide-like waves. Hence, our results complement and extend the observational study of Hibbins et al. (2019) using SuperDARN and the model study of Limpasuvan et al. (2016) based on WACCM as well as the work of He and Chau (2019) using SMR. In confronting model results against observations, this study may also illuminate the potential role of model biases in simulating tides. To date, in the literature, various authors have reported model results on the behavior of semidiurnal tides during SSWs. However, their results focus on individual SSW events instead of a composite as done here (Pedatella et al., 2016, 2014; Sassi et al., 2013; Siddiqui et al., 2019), are based purely on model simulations (Pedatella et al., 2012), or are limited to model comparison with single-station observations that do not resolve tidal zonal wavenumbers (e.g., Conte et al., 2019).

## 2. Data and Methods

### 2.1. Model: SD-WACCM-X

With a top boundary between 500 and 700 km (depending on solar and geomagnetic activities), the NCAR CESM2.0 WACCM-X includes representations of physical processes found in WACCM which has a model top around 130 km. It has a revised parameterized non-orographic gravity wave forcing described by Garcia et al. (2017) and treatment of surface stress due to unresolved topography that significantly improves the SSW frequency of occurrence (Richter et al., 2010). With its new release, WACCM-X now incorporates additional processes (like neutral wind dynamo, ionospheric transport, and calculations of ion/electron energetics and temperatures) to better resolve the thermospheric energetics and thermal structure. Along with the integration of additional processes found in the NCAR Thermosphere-Ionosphere-Electrodynamics General Circulation Model (TIE-GCM; Qian et al., 2014), WACCM-X can self-consistently resolve lower atmospheric processes (Liu et al., 2018), and can provide a more realistic simulation of upper atmospheric variability due to lower atmospheric forcing. The finite volume dynamical core (FV dycore) in WACCM-X accounts for species-dependent specific heats and mean molecular weights. The updated FV dycore prevents unrealistic and excessive large mean meridional and vertical winds and temperature in the thermosphere while generating more realistic tidal structures (more details provided in Liu et al., 2018).

The WACCM-X simulations were performed at NCAR using the specified dynamics configuration (hereafter, referred to as SD-WACCM-X). The hourly output from SD-WACCM-X from 2000–2014 (the CESM run f. e20. FXSD.f19\_19.001 data) was accessed through Earth System Grid (<https://www.earthsystemgrid.org>). In this configuration, the model's temperature, surface pressure, and wind fields are constrained below 50 km by NASA Modern-Era Retrospective Analysis for Research and Application (MERRA2; Gelaro et al., 2017). Above 60 km, the model is fully interactive and free running. Unlike other models released with CESM2.0, the horizontal resolution of SD-WACCM-X remains the same as its predecessor at 1.9° latitude by 2.5° longitude.

### 2.2. Observations: SuperDARN and SKiYMET

Operating since 1993, the high-frequency radars in the SuperDARN network remotely detect ionospheric plasma convection, upper atmospheric clouds, and neutral winds. Based on the multi-pulse sounding technique of Farley (1972), these radars infer neutral winds from trails of ablated meteors around 95 km (Hall

et al., 1997). The measured winds represent a vertical average over an approximate 10-km layer centered near 95 km. Eight SuperDARN radar stations are located between 150.1°W and 25°E in the 50°N–66°N latitude band: Hankasalmi (HAN: 25.2°E, 64.4°N), Pykkvibaer (PYK: 18°W, 65.7°N), Stokkseyri (STO 26.9°W, 64.7°N), Goose Bay (GBR: 60.3°W, 55.5°N), Kapuskasing (KAP: 83.3°W, 51.4°N), Saskatoon (SAS: 105.2°W, 54.2°N), Prince George (PGR: 123.2°W, 56.1°N), and Kodiak (KOD: 150.1°E, 59.5°N). Hibbins et al. (2019) used meteor wind data from these radars to perform a non-linear least-square surface fit in longitude and time on simultaneous measurements of hourly mean horizontal winds over this relatively narrow latitude band. The fit covers a sliding 4-days data period. Despite missing data coverage over Russia that spans over 100° in longitude, these authors successfully extracted daily mean wind, migrating diurnal tides, and migrating and non-migrating semidiurnal tides (reliably up to zonal wavenumber 3). The amplitude and phase of planetary-scale tidal winds can be obtained by fitting daily winds as a function of longitude. By similar fitting techniques, observations from the same eight SuperDARN stations have been used to infer PW climatology and variability (Kleinknecht et al., 2014; Stray et al., 2015a, 2015b). Here, we utilize the derived SuperDARN data between 1995 and 2016, as in Hibbins et al. (2019).

Additional observations are provided by the All-Sky Interferometric Meteor Radar (SKiYMET; Hocking et al., 2001) at Trondheim, Norway (63.4°N and 10.5°E). Operated by the Norwegian University of Science and Technology (NTNU) since 2012, this SKiYMET radar consists of eight transmitting antennas, phased to transmit most of the power at zenith angles between 15° and 50°. Over this site, the maximum meteor count rates occur around 90 km with an average daily count rate of around 6,500 unambiguous meteors between 70 and 100 km. The system can infer neutral winds between 80 and 100 km from meteor trails. Methods described by De Wit et al. (2014) are used to process the neutral wind. Lacking the constraints to an optimal retrieval altitude like SuperDARN (i.e., at ~95 km), SKiYMET provides an altitude-time evolution of horizontal winds between 80 and 100 km at around 4 km vertical resolution.

### 2.3. Data Analysis

For SD-WACCM-X, we apply two-dimensional Fast Fourier Transform (2D FFT) to isolate semidiurnal variations and other wave signatures in the hourly data. The time series centered over each selected year comprise 90 days before the first day of January of that year and 90 days after the last day of December of that same year, yielding a series of nearly 545 days long. A Tukey window is applied to the time series to taper 90 days before and 90 days after the selected year. The long series length provides a spectral frequency resolution of  $\sim (545 \times 24)^{-1}$  cycles per hour (cph) to isolate signals in relatively narrow period bands. After band-passing for a desired signal in the frequency domain (the bandpass range is described in the next two paragraphs), the filtered data before January 1 and after December 31 are discarded. When placing the filtered data over consecutive years, discontinuity from one year to the next was verified to be negligible. We note that tidal signatures can be obtained by least-square fitting (e.g., Wu et al., 1995). The least-square fitting method is suitable to handle irregular sampling data, such as satellites, whereas 2D FFT is the common approach for regularly gridded model data. For tidal signatures, we nevertheless verified that the filtered signatures from 2D FFT are similar to those derived from least-square fitting.

Based on the sliding 4-days (hourly) data window, the results extracted from SuperDARN are expected to capture a broader range of perturbations than just those with purely semidiurnal characteristics. For a 4-days window length, the frequency resolution in Fourier Analysis comparable to the least-square fitting is roughly 1/96 cph. Hypothetically, such a resolution in FFT yields less than 3 Fourier coefficients to estimate semidiurnal variation centered within a 10–14-h period band. While the longer model data time series discussed above yields a much higher frequency resolution, we initially apply the broad 10–14-h period band filter to extract SW1, SW2, and SW3 in SD-WACCM-X to facilitate a comparison with the semidiurnal tides derived from SuperDARN in Section 3.

The finer spectral resolution afforded by the long model time series allows us to examine SW1, SW2, and SW3 at a much narrower period band. When focusing solely on the model results (as done in Section 4), we present model results for these semidiurnal tides filtered between 11.8 and 12.2 h which is comparable to that of He and Chau (2019). If the non-linear interaction between QSPW1 (say, slower than 30 days) and SW2 were to occur, this period band would accommodate the resultant SW1 and SW3 products. The finer

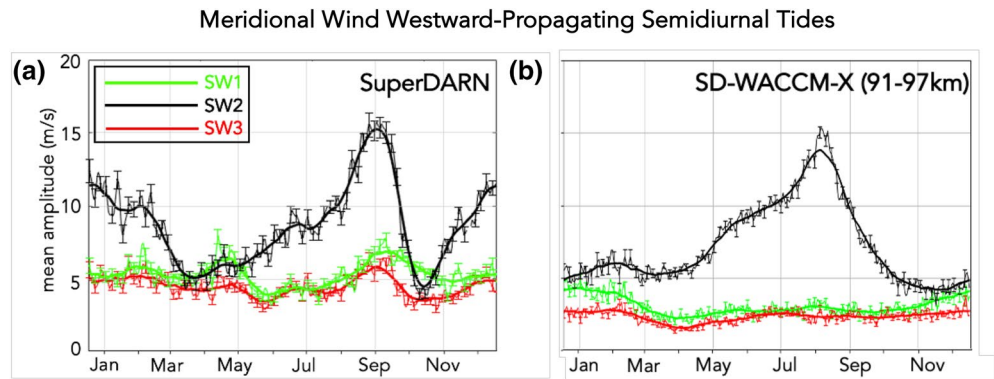


**Figure 1.** Climatological evolution of three westward-propagating semidiurnal tidal components for (a) SuperDARN and (b) SD-WACCM-X averaged between 91 and 97 km altitude band. Black curves show the migrating component (SW2), green and red curves show the wavenumber 1 and wavenumber 3 non-migrating components (SW1 and SW3), respectively. SuperDARN results are computed from eight stations located between 51°N and 66°N around the globe. The vertical bars indicate the standard errors. The SD-WACCM-X results are computed from all model grids in the same latitude. The vertical bars indicate the standard error of interannual variability, which is the standard deviation divided by the square root of the number of years. The bold lines represent the 30-days running mean.

band-pass filtering also allows us to extract semidiurnal-tide-like wave ( $\tilde{S}W1$  and  $\tilde{S}W3$ ) at nearby 12-h oscillatory period, that may have been included with the observed and broad-band filtered results of SW1 and SW3 (in Section 3). As noted in the Introduction,  $\tilde{S}W1$  and  $\tilde{S}W3$  may result from the interactions between SW2 and westward traveling PW with periods between 10 and 20 days (i.e., WPW1). To accommodate for this possible interaction,  $\tilde{S}W1$  and  $\tilde{S}W3$  are derived by filtering for zonal wavenumbers 1 and 3 over a period range of 12.31–12.63 h and 11.43–11.71 h, respectively. Again, these period bands are comparable to those of He and Chau (2019). We note that, in using these narrow period ranges (all with a similar frequency bandwidth of  $\sim 0.002 \text{ h}^{-1}$ ), the temporal resolution of the bandpassed amplitudes would be reduced. Their time variation will be roughly 10 days or slower and smoother than the results of the wider period band (10–14-h). Finally, the QSPW1 and WPW1 signatures are obtained by band-pass filtering for zonal wavenumber 1 with periods longer than 30 days and for periods between 10 and 20 days, respectively. For all model results, the statistical significance is tested by the Student's *t*-test.

### 3. A Comparison of SuperDARN and SD-WACCM-X

#### 3.1. Climatological Westward-Propagating Semidiurnal Tides

Figure 1 illustrates the annual climatology of SW1, SW2, and SW3 meridional wind amplitudes from SuperDARN in panel (a), based on the 1995–2016 period, and SD-WACCM-X in panel (b), based on the 2000–2014 period, near 95 km. The observed SW2 variation (black line in Figure 1a) exhibits a maximum peak around  $15 \text{ m s}^{-1}$  in early September and a secondary peak around  $12 \text{ m s}^{-1}$  at the end of the year. Overall, SW2 dominates the non-migrating components during much of the year, except around April and October. During these two periods, the SW2 amplitude dips to around  $5 \text{ m s}^{-1}$  and briefly below SW1 (green line). The SW1 and SW3 amplitudes hover around  $5 \text{ m s}^{-1}$  throughout the year. Overall, the climatology is similar to the midlatitudes observations ( $49 \pm 8.5^\circ\text{N}$ ) of He and Chau (2019) using a network of five SMRs. However, their SMR SW2 climatology (averaged between the altitude of 80 and 98 km) is always above  $7 \text{ m s}^{-1}$  and consistently dominates SW1 and SW3.

Based on observations from NASA's Sounding of the Atmosphere using Broadband Emission Radiometry (SABER), Truskowski et al. (2014) indicated a similar peak activity in SW1 and SW3 temperatures in September–October in the northern subtropics to mid-latitudes, with a secondary peak in April for the SW1 case. The non-linear interaction between QSPW1 and SW2 may explain the climatological autumnal SW1 and SW3 maxima. Stray et al. (2015b) observed a QSPW1 in SuperDARN in July, using the same stations and similar techniques employed here. While direct upward propagation of QSPW1 from below the MLT

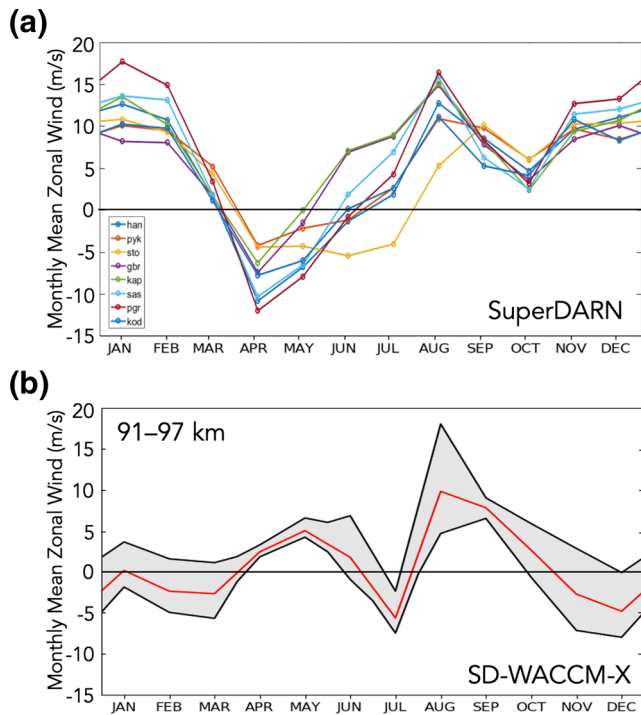


**Figure 2.** Climatology of monthly mean zonal wind for (a) SuperDARN and (b) SD-WACCM-X. In (a), each circle indicates values at each of the eight stations noted in the legend. In (b), the red curve represents zonally averaged values between 51°N and 66°N and between 91 and 97 km. The gray region denotes maximum and minimum range of zonal wind values between the averaged latitude band.

climatology of zonal wind for the individual SuperDARN stations is shown in Figure 2a. Collectively, the high-latitude zonal wind at this altitude is eastward most of the year, except between Spring and early Summer. In comparison with Figure 1a, we see a strong temporal correlation between the observed SW2 amplitudes and the climatological zonal wind. For example, both tend to peak around August and minimize around April (when the wind is predominantly westward) and early November. During the latter two months, when the SW1 amplitude can exceed SW2 in SuperDARN, the radar climatological zonal winds are at their relative minima.

In their multi-model comparison of the 2009 SSW simulations, Pedatella et al. (2014) noted the diversity of model background zonal wind in the lower thermosphere. The monthly mean SD-WACCM-X zonal-mean zonal wind values (averaged between the 91–97 km altitude range) gridded between 51°N and 66°N are plotted in Figure 2b for comparison with SuperDARN winds. The red curve indicates the average values, and the gray region illustrates the value range over the latitude band. The monthly mean zonal wind in SD-WACCM-X differs significantly from SuperDARN. Namely, the simulated climatological wind is predominantly westward during the year, being weakly eastward only during April–May and August–September. Like the observed behavior, the modeled SW2 amplitude shown in Figure 1b maximizes with the eastward wind peak around August. The lack of strong secondary SW2 amplitude maximum toward the end of the year in the model may be associated with the absence of persistent eastward wind found in observations. Similarly, the lack of strong springtime westward wind in the model seems to coincide with the weakened SW1 amplitude in contrast to observations. We also note that, although the zonal-mean zonal winds are in good agreement during the early Fall, the simulated SW1 and SW3 are still weak compared to observations.

The climatological zonal wind difference between model and observations is further highlighted in Figure 3. Panel (a) shows the altitude-time evolution of the climatological daily annual cycle of the zonal wind averaged over 2013–2019 from the NTNU SKiYMET radar, and panel (b) the corresponding SD-WACCM-X zonal wind (but for 2000–2014) at the same location as SKiYMET. The SKiYMET zonal wind above 88 km

is unlikely, these authors suggested that QSPW1 features may result from the longitudinal differences in tropospheric gravity wave sources, barotropic and baroclinic instabilities as well as inter-hemispheric propagation from the Southern Hemisphere (Espy et al., 1997; Hibbins et al., 2009). In April, QSPWs associated with the stratospheric final warming may again interact with SW2, whose growth recurs in Spring, to spawn SW1 and SW3. Alternatively, the non-linear interactions between westward-propagating diurnal tides of zonal wavenumbers 1 and 2 can theoretically lead to the seasonal climatological variation of SW3 (Sridharan, 2019), along with the changing tropospheric forcing below.

The corresponding SD-WACCM-X results are shown as averaged values within the 51°N–66°N latitude band where the SuperDARN stations are located and within 91–97 km altitude range in Figure 1b. The results shown are not sensitive to slightly varying the altitude and latitude averaging bands. The simulated SW2 amplitude exhibits a primary peak before autumn with slightly smaller amplitude than observed, and two minima around a similar time of the year as in the observations. The secondary SW2 peak in the model is more diminutive and appears later in the winter. Like SuperDARN, the simulated SW2 amplitude dominates the non-migrating amplitudes. However, the non-migrating amplitudes are smaller than observations, and the growth and dominance of SW1 around May and October observed in SuperDARN are not captured in SD-WACCM-X.

Differences noted in Figures 1a and 1b may be attributed to the contrasting zonal wind behaviors between observations and model. As noted in previous studies (Conte et al., 2019; Jin et al., 2012; Pedatella et al., 2012; Sassi et al., 2013; Siddiqui et al., 2019), the response of semidiurnal tides is sensitive to the background zonal wind. The observed monthly mean

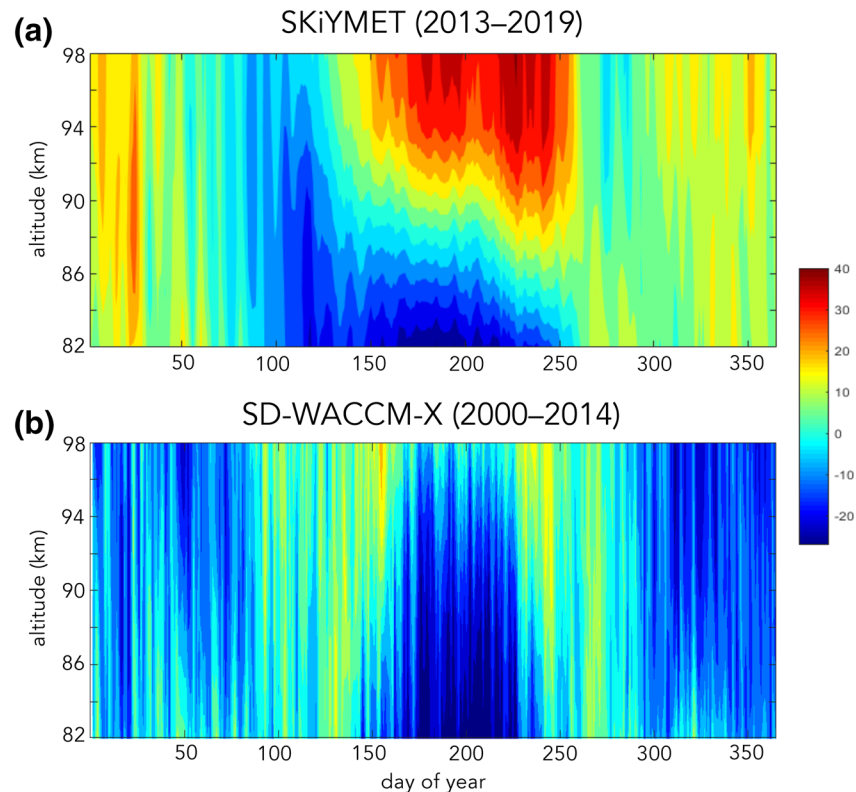


**Figure 3.** Altitude versus time annual climatology of zonal wind for (a) the NTNU SKiYMET radar at 63.4°N and 10.5°E and for (b) SD-WACCM-X at the same geographical location. The climatology is computed from 2013 to 2019 for SKiYMET and from 2000 to 2014 for SD-WACCM-X.

is eastward (warm color) most of the year, except for days between 80 and 130 (between March and May). This behavior is consistent with the SuperDARN observations (Figure 2a). At lower altitude, westward wind (cool color) dominates the annual cycle with minimum values of  $-20 \text{ m s}^{-1}$  around July. As seen in panel (b), the local zonal wind in the model is markedly different from observations. Namely, the presence of westward wind is more prevalent at these altitudes than the observations reveal. Eastward wind tends to only appear around late Spring and early Fall, while observations show prevailing eastward wind from day 130 onwards above 88 km.

In summary, the amplitudes of westward-propagating semidiurnal tides between model and observations bear some likeness. The strongest similarity is evident in SW2, especially with an amplitude peak around early Fall in coincidence with strong eastward lower-thermospheric winds. Contrasting zonal wind behavior during other seasons may contribute to different tidal behaviors.

### 3.2. Westward-Propagating Semidiurnal Tides during SSWs

We now compare the composite behaviors of SW1, SW2, and SW3 for 9 SSW events in SD-WACCM-X (between 2000 and 2014) with the corresponding composite for 13 SSW events in SuperDARN (between 1995 and 2016) reported in Hibbins et al. (2019). For robustness, we chose to build composites using the maximum number of available SSW events within the model and observation records, rather than to compare the exact same events. The SSW onset dates are taken from Limpasuvan et al. (2016) for persistent SSW events (defined at 1 hPa) with an elevated stratopause. Before compositing, each SSW event is aligned with respect to its onset date (defined to be day 0) during which the polar cap zonal mean zonal wind reversal occurred at 1 hPa. The composite smooths and weakens the amplitude but is used here to reveal the robust response to SSW. In the model, all SSW events are weighted equally. However, hourly radar winds during each event in SuperDARN are weighted by a measure of data standard deviation as further explained in Hibbins et al. (2019).

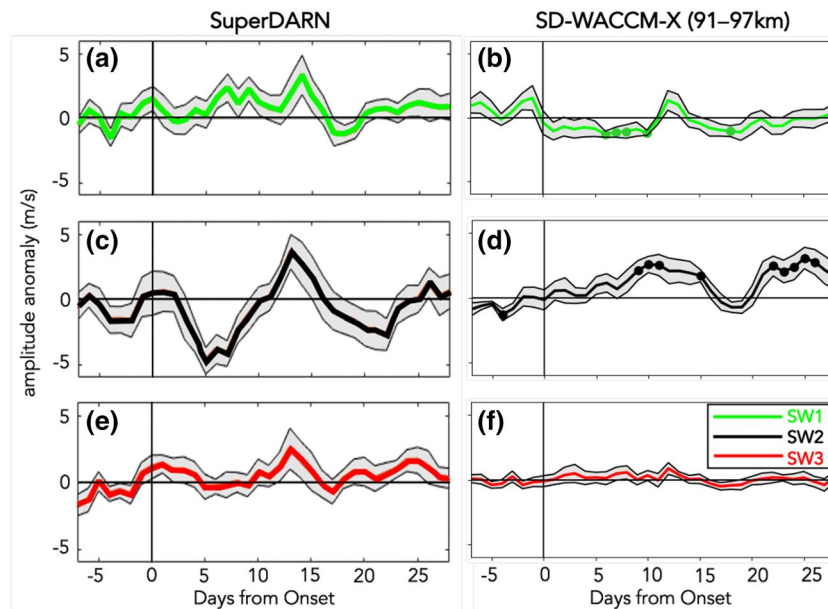


**Figure 4.** Amplitude anomaly composites during SSWs plotted across onset (day 0) for SW1, SW2, and SW3 for SuperDARN (left column) and SD-WACCM-X (right column). For SuperDARN, the gray region denotes the standard error of the weighted mean. For SD-WACCM-X, the gray region denotes the standard error of event-to-event variability. The SuperDARN composite is based on 13 SSW events between 1995 and 2016. The SD-WACCM-X composite is based on 9 SSW events between 2000 and 2014. The filled circles in the right column indicate where the  $t$ -test statistical significance level is above 95%.

Figure 4 illustrates the time evolution of the composite meridional wind amplitude anomalies for SW1, SW2, and SW3, starting from 7 days before SSW onset (day 0) to 28 days thereafter. Here, we define the amplitude anomaly as the departure from the 30-days smoothed climatological values which, between December and March when SSWs typically occur, are between 5 and 13  $\text{m s}^{-1}$  (see Figure 1 bold lines). Each tidal component is separated by rows and colored as in Figure 1. The 13 individual time evolutions of the meridional wind amplitude anomalies can be seen in Hibbins et al. (2019) as their Figure 7.

The observed results indicate a strong positive anomaly in unison for all components between days 10–15 after SSW onset, with SW2 peaking on day 13. The model results at the SuperDARN altitude show a very small positive response in SW1 and SW3 and a weak enhancement in SW2 around the same period. A near-doubling of the SW2 amplitude about two weeks after the SSW onset in SuperDARN is consistent with the case study of the 2012–2013 SSW in Orsolini et al. (2017) and with other studies (Conte et al., 2019; Pedatella et al., 2016, 2012; Sassi et al., 2013; Siddiqui et al., 2019). The SW2 amplitude becomes anomalously low after day 17, then enhances again after day 24 in the observations. The simulated SW2 anomaly is also negative after day 15 but becomes positive before day 20.

Prior to the initial amplification, the observed SW2 amplitude shows a negative anomaly (maximum at day 5) that is, absent in the model. An amplitude decrease in SW2 early in the SSW development has been reported previously by Chau et al. (2015), Conte et al. (2019), Pedatella et al. (2012), Sassi et al. (2013), and Wang et al. (2011).

## 4. Semidiurnal Tides and Semidiurnal-tide-like Wave in SD-WACCM-X

### 4.1. Climatological Semidiurnal Tides and Semidiurnal-tide-like Wave

Figure 5a illustrates the SW1, SW2, and SW3 climatology in SD-WACCM-X like Figure 1b but for the narrower band filter (see Section 2.3). For clarity, only the 30-days running mean values are shown. We see that the refined SW2 annual climatology (solid black line) remains nearly the same as the broader band results in Figure 1b. However, the refined SW1 amplitude (solid green line) and SW3 amplitude (solid red



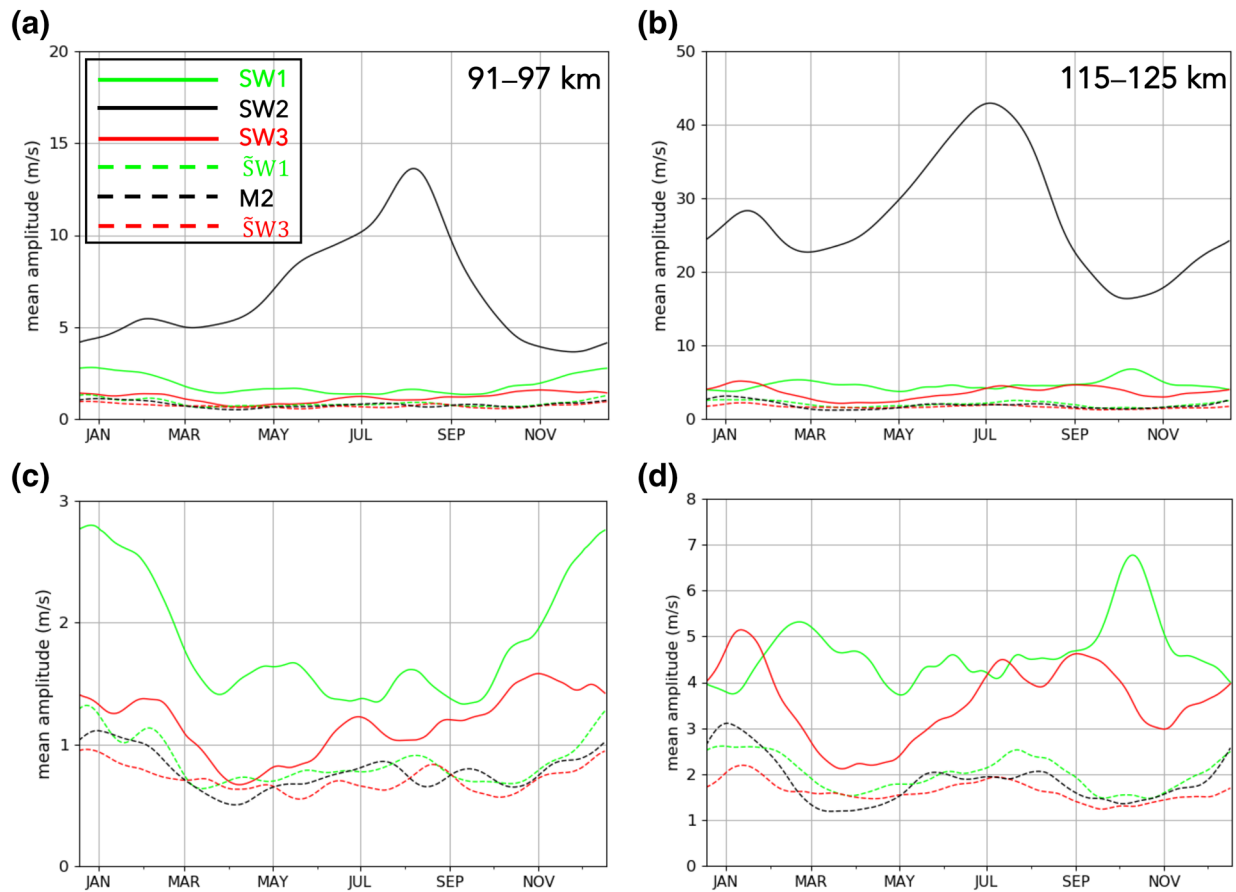


**Figure 5.** Climatological evolution of SW1, SW2, SW3, semidiurnal-tide-like wave signatures ( $\tilde{S}W1$  and  $\tilde{S}W3$ ), and migrating semidiurnal lunar tide (M2) in SD-WACCM-X averaged between 51°N and 66°N for the altitude averaged band of (a) 91 and 97 km and (b) 115 and 125 km. Detailed variations of non SW2 signals are shown in panel (c) and (d). All lines represent the 30-days running mean.

line) are smaller by 1–2 m s<sup>-1</sup>. Further highlighted in Figure 5c, SW1 still dominates over SW3 throughout the year, peaking between late Fall through Winter (consistent with Figure 1b). Also shown are the  $\tilde{S}W1$  and  $\tilde{S}W3$  climatologies in dashed green and red lines, respectively. These semidiurnal-tide-like wave amplitudes are even smaller than the pure non-migrating semidiurnal tides but tend to maximize around Winter. The right column of Figure 5 repeats panels (a) and (c) but for the 115–125 km altitude range. The climatological wave amplitudes are all stronger at this higher altitude. The refined SW2 now exhibits a summertime peak slightly earlier than at lower altitude, and a secondary peak is more evident in mid-January. The annual variation of SW3 at these levels (Figure 5d) is more comparable to SW1, and the peaks of  $\tilde{S}W1$  and  $\tilde{S}W3$  tend to occur around January. As explored below, this higher altitude range captures the much stronger response of semidiurnal tides and semidiurnal-tide-like wave in the model during SSWs.

Analogous to Figures 4b, 4d, 4f, Figures 6a, 6c, and 6e capture the composite responses of the refined SW1, SW2, and SW3 (solid lines) during SSWs averaged between 91 and 97 km. In Figure 6a, the anomalous reduction in SW1 occurs over an extended time period after SSW onset, which is not evident in Figure 4b. For the refined SW2, the enhancement around day 10 is not as pronounced as in Figure 4d. The diminished response is perhaps expected for the narrower filter band compared to the broader band used in the previous section. The latter would include, in addition to SW2, possible small wavenumber-2 perturbations with periods near 12 h that are model-generated manifestations (such as M2, discussed in Section 4.5) and are theoretically possible (e.g., Forbes et al., 2012). These perturbations could potentially interfere to yield a slightly larger broad-band response and at a slightly different time. The SW3 response is generally small, as also noted in Figure 4f. Overall,  $\tilde{S}W1$  and  $\tilde{S}W3$  (dashed lines) during SSW are smaller than 0.3 m s<sup>-1</sup> at this altitude range. Nonetheless, their respective superposition with SW1 and SW3 may be reflected in the signatures shown in Figures 4b and 4f.

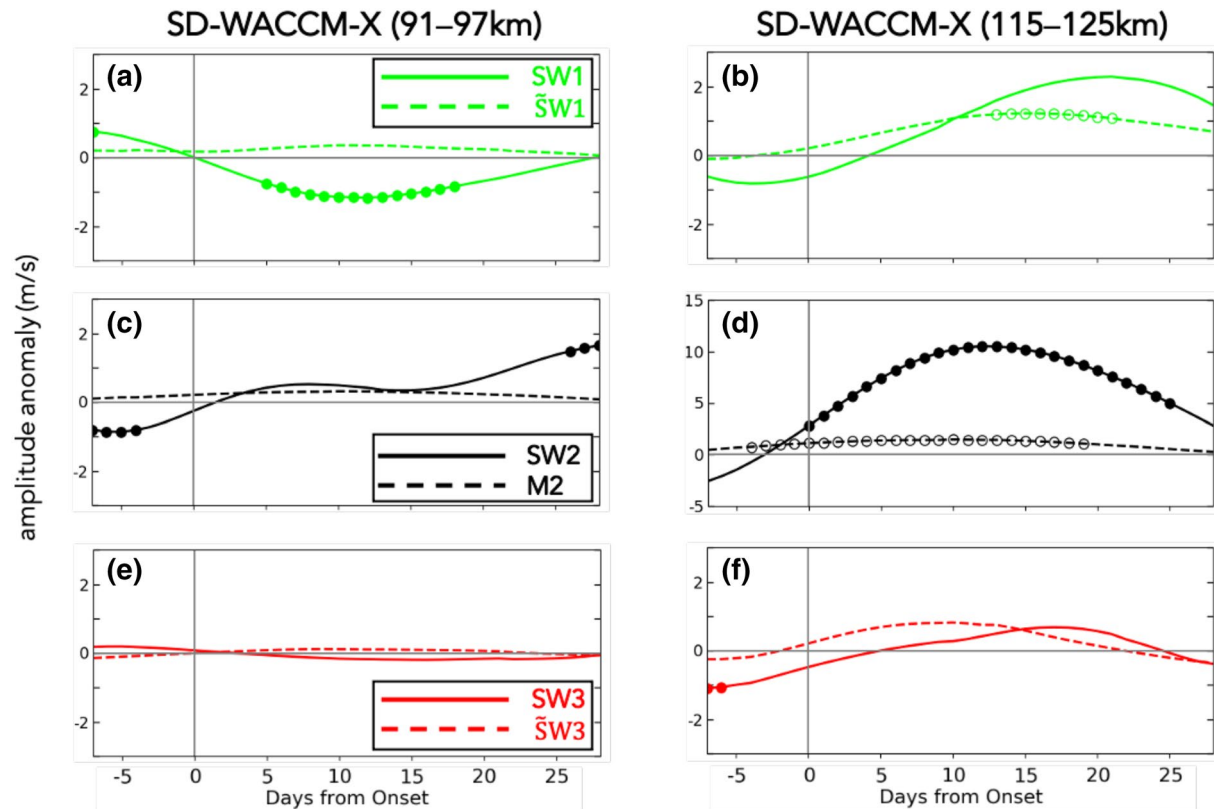


**Figure 6.** Amplitude anomaly composites during SSWs plotted across onset (day 0) for SW1 and  $\tilde{S}W1$  (a) & (b), SW2 and M2 (c) & (d), and SW3 and  $\tilde{S}W3$  (e) & (f). The left column shows the altitude averaged band of 91 and 97 km and the right column for 115 and 125 km. The composite is based on 9 SSW events between 2000 and 2014. Note in (d) that the y-axis is different from others. The filled (unfilled) circles indicate where the *t*-test statistical significance level is above 95% for SW1, SW2, and SW3 ( $\tilde{S}W1$ , M2 and  $\tilde{S}W3$ ).

Between 115 and 125 km (Figures 6b, 6d and 6f), we see stronger responses to SSW. This is especially so in SW2 between day 5–15 (note the new ordinate range in Figure 6d). The responses of SW1 and SW3 tend to enhance after day 10. Prior to day 10, at this altitude the modeled  $\tilde{S}W1$  and  $\tilde{S}W3$  anomalies can in fact be larger than those in SW1 and SW3, as discussed in He and Chau (2019). We also note an anomalous decline prior to onset for SW2 and even up to day 5 for SW1 and SW3.

#### 4.2. Global SW2 Behavior during SSWs

Figure 7 shows the composite latitude-altitude structure of SW2 meridional wind amplitude (top row) and the amplitude anomaly (middle row). The response to SSW onset is illustrated by 10-days averages from day –11 to –1 and from day 5–15 with respect to SSW onset (left and right column, respectively). Days 5–15 are used to capture the strong SW2 growth seen in Figures 6d. The stippled areas indicate where the anomalies are statistically significant at the 95% level. In general, the SW2 amplitude at each altitude tends to minimize over the equatorial region. At each latitude, the amplitude grows rapidly with altitude. The overall structure is dominated by two extrema in the mid-latitudes of both hemispheres above 100 km. To accentuate the weaker amplitude below 100 km, contours (every  $1 \text{ m s}^{-1}$ ) are shown as dashed lines. The summertime thermospheric amplitude peak is about 10 km higher than the wintertime peak and roughly twice as large. Below 100 km, the wintertime amplitude tends to be larger than the summertime counterpart. After SSW onset (comparing Figure 7a with Figure 7b), the mid-latitude thermospheric SW2 maxima grow by more than 30% in each hemisphere.

With the climatology removed prior to compositing, we see significant anomalous SW2 response to SSW (Figures 7c and 7d). Before SSW, the anomalous structure is confined to mainly above 90 km with weaker than normal amplitudes over the equatorial region near the mesopause that extend toward higher latitudes

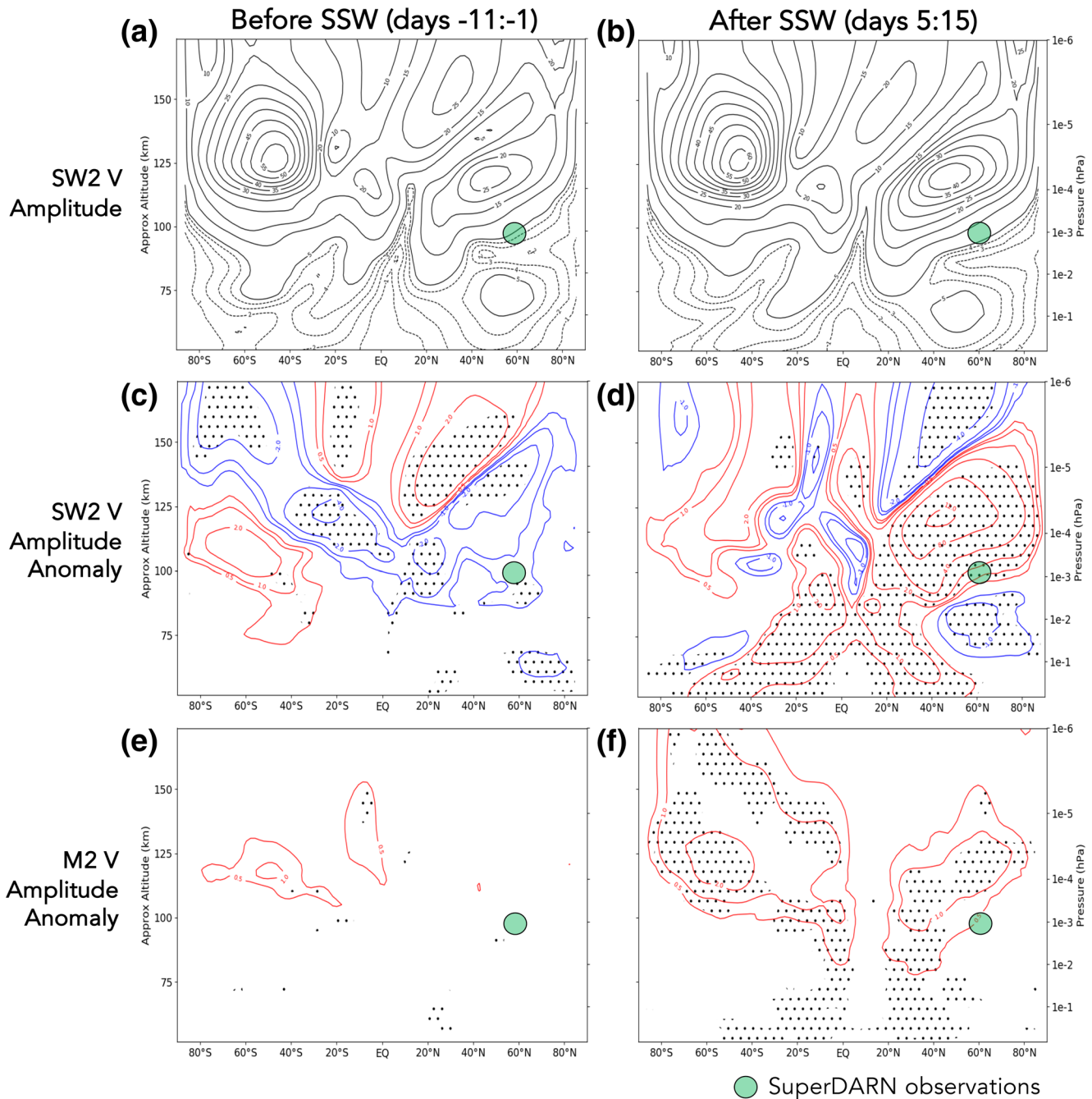


**Figure 7.** Top row (a), (b) shows the altitude-latitude composite structure of the migrating semidiurnal tide (SW2) meridional wind amplitude during the 10-days averaged period before (left) and after (right) SSW onset. Solid contours are provided every  $5 \text{ m s}^{-1}$  and dashed contours every  $1 \text{ m s}^{-1}$  to accentuate smaller values. Middle row (c), (d) shows the corresponding plots for SW2 meridional wind amplitude anomaly. Bottom row (e), (f) shows the corresponding plots for M2 meridional wind amplitude anomaly. The anomaly is defined as a departure from the climatological mean. Red contours show the positive anomaly and blue contours show the negative anomaly, contoured at  $0.5, 1, 2, 4, 8, 12 \text{ m s}^{-1}$ . Stippling shows where the  $t$ -test statistical significance level is above 95%. The green dot locates the approximate region of the SuperDARN observations.

while ascending in altitude. The significant negative anomaly is typically less than  $3 \text{ m s}^{-1}$ . After SSW, the anomalous SW2 amplitude becomes overwhelmingly positive, particularly in the winter hemisphere above 90 km, and consistent with the amplitude enhancement noted in Figure 6d. Peak amplitude anomalies appear near  $40^\circ\text{N}$  and around 125 km. The weak decrease in SW2 from low-to mid-latitudes above 100 km prior to onset becomes confined around the equatorial region after the SSW onset. The altitude sampled

by the SuperDARN radars (green circles) lies between height ranges where the model SW2 amplitude has increased or decreased SW2 (Figures 7d), which could explain the weak modeled increase after SSW onset in Figures 4d and 6c.

Figure 8a shows the latitude-time evolution of the anomalous SW2 amplitude in the model, averaged over 91–97 km. Between 51°N and 66°N where the SuperDARN stations are located, we see a consistent evolution in Figure 8a that explains the two maxima in Figure 6c. The positive anomalies persist more than one month with peak amplitude around day 30. The stronger SW2 enhancement after SSW onset in the Northern Hemisphere actually appears at lower latitudes. Significant low-latitude negative anomalies (albeit weak) are also evident before SSW onset, consistent with Figure 6a.

The latitude-time evolution of anomalous SW2 amplitude averaged between 115 and 125 km is illustrated in Figure 9a. Consistent with Figures 6b and 6a large positive enhancement occurs in the mid- to high winter latitude after SSW onset, peaking around day 15 and lasting thereafter for nearly 3 weeks. The wintertime enhancement occurs after the strong positive SW2 anomaly in the Southern Hemisphere (peaking around day 3). This strong summer SW2 anomaly appears to be modulated by an equatorward propagating oscillation of about 20 days from the Northern Hemisphere. Prior to SSW onset, the anomalies are negative in the Northern Hemisphere and are statistically significant over some instances. The development of the global SW2 structure in SD-WACCM-X is consistent with the case studies of the 2009 SSW by Sassi et al. (2013) using an older version of SD-WACCM-X and Jin et al. (2012) using the Ground-to-topside model of Atmosphere and Ionosphere for Aeronomy (GAIA) model, and with the SSW composite of Pedatella et al. (2012) using WACCM.

We examine the changes in SW2 wave activity flux (WAF) before and after SSW onset in Figures 10a and 10b, respectively. The WAF vector is normalized in length but colored to show its magnitude. In general, SW2 wave activity emanates from below 100 km in the Northern Hemisphere tropical region, indicative of tropical ozone heating in the stratosphere as a source for SW2. The wave activity then diverges meridionally toward the mid-latitude region of both hemispheres between 100 and 125 km. In the Southern Hemisphere, the wave activity amplifies with extended upward propagation to 175 km. In the Northern Hemisphere, vertical wave propagation is limited to around 125 km, a similar finding was shown in the WACCM-based results of Pedatella et al. (2012).

Over the displayed altitude range, in addition to dissipation by wave breaking, molecular diffusion can become effective at damping wave growth. Correspondingly, mid-latitude Eliassen-Palm (EP) flux convergence (and associated westward momentum forcing contoured with dashed lines) is evident in the Southern Hemisphere above 100 km and in the Northern Hemisphere above 125 km. Overall, the uneven upward penetration of wave activity in this altitude range appears consistent with the SW2 amplitude structure (see Figure 7, top row). The prevalence of SW2 wave propagation from the tropics into the Southern Hemisphere between 110 and 125 km also accounts for the earlier occurrence of anomalous SW2 amplitude in the Southern Hemisphere shown in Figure 9a.

The SW2 response to SSW is quite dramatic in Figure 10b. Equatorial vertical upwelling of WAF appears stronger in the upper mesosphere, as evidenced by the appearance of red/orange vectors and EP flux vectors emanating from a slightly lower altitude (~75 km). Enhanced energy propagation into each hemisphere also occurs, giving rise to strong EP flux convergence in the winter lower thermosphere. Around 30°N and 112 km, westward SW2 tidal forcing after SSW is nearly twice the magnitude before SSW. However, below 130 km, SW2 westward forcing does not penetrate into the winter polar region. Interestingly, the EP flux patterns consistently show strong flux divergence over the polar region, as also found in Pedatella et al. (2016).

The changes in QSPW1 WAF due to SSW onset are shown in Figures 10c and 10d. We verified that the total QSPW (zonal wavenumbers 1–5) is dominated by QSPW1. QSPW1 activity emanates from the winter lower stratosphere and is refracted equatorward with EP flux convergence near the midlatitude stratopause. The WAF then continues to propagate upward and equatorward, converging in the middle mesosphere. The presence of wintertime QSPW1 in the MLT has been readily observed in satellite observations

91–97 km

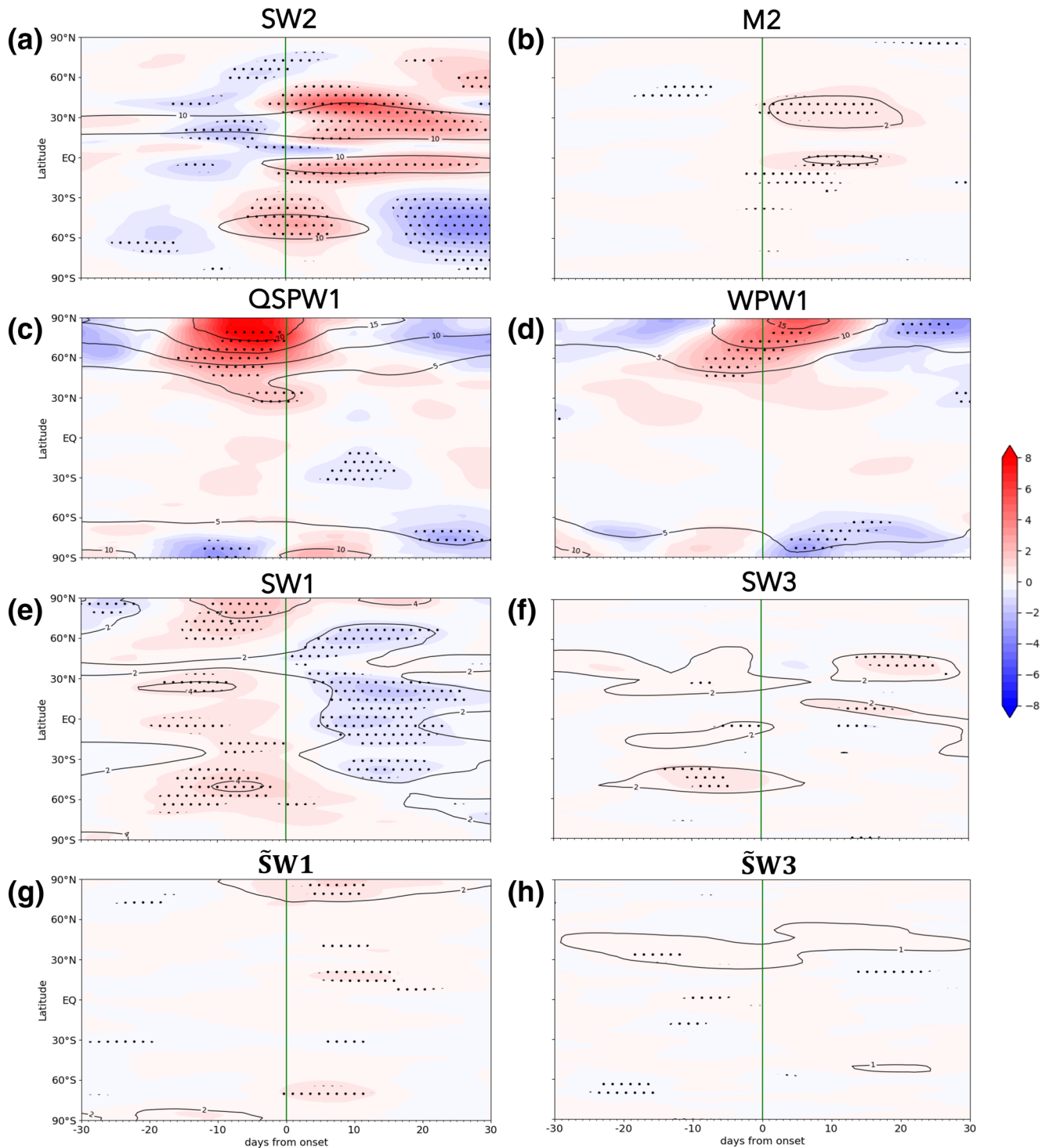


**Figure 8.** Latitude-time distribution of the composite meridional wind amplitude (line contours) and its anomaly (filled contours), averaged between 91 and 97 km, for (a) SW2, (b) M2, (c) QSPW1, (d) WPW1, (e) SW1, (f) SW3, (g)  $\tilde{S}W1$ , and (h)  $\tilde{S}W3$ . The time is shown with respect to SSW onset (day 0, green line). Stippling indicates where the *t*-test statistical significance level is above 95%.

115–125 km

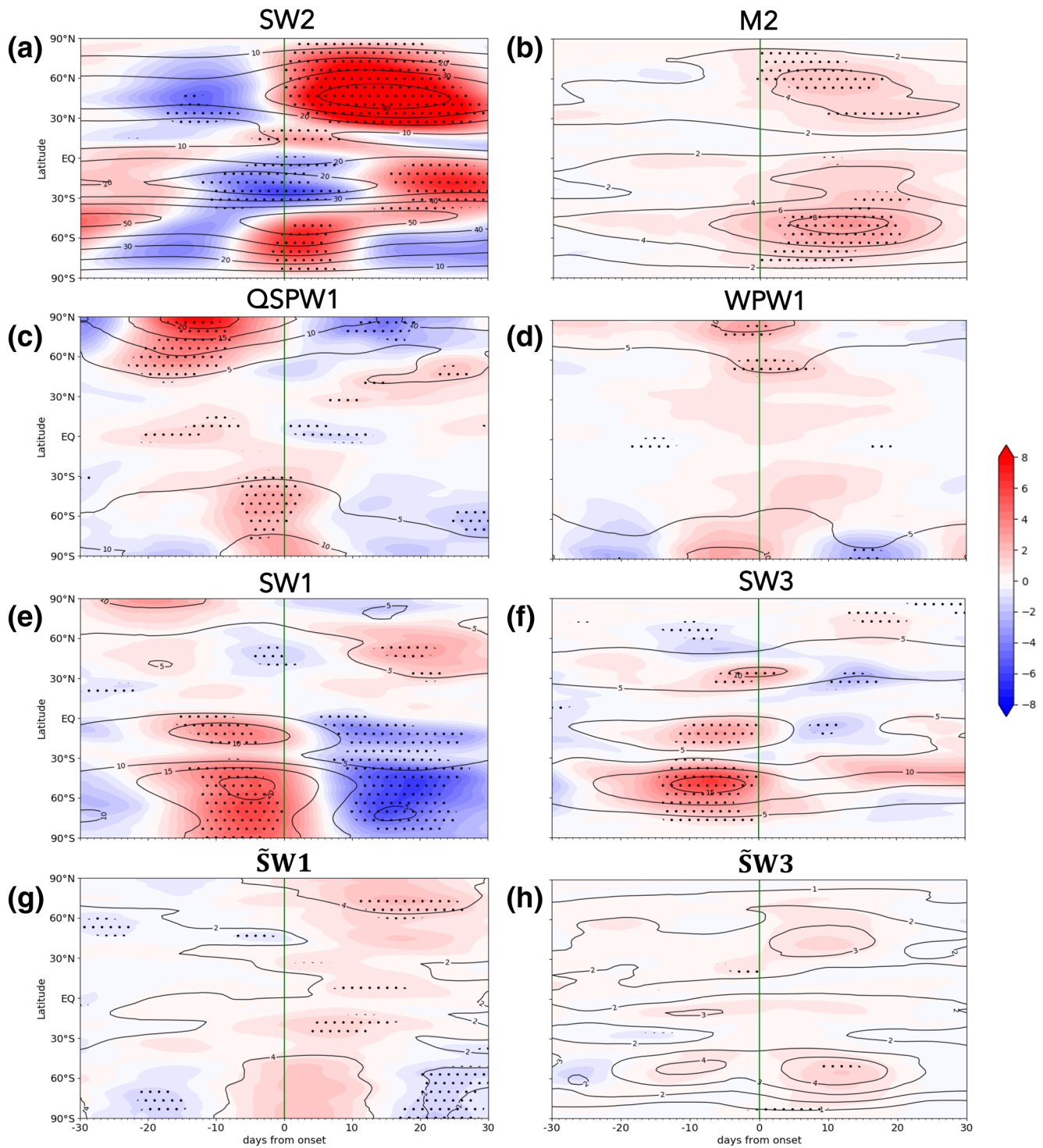
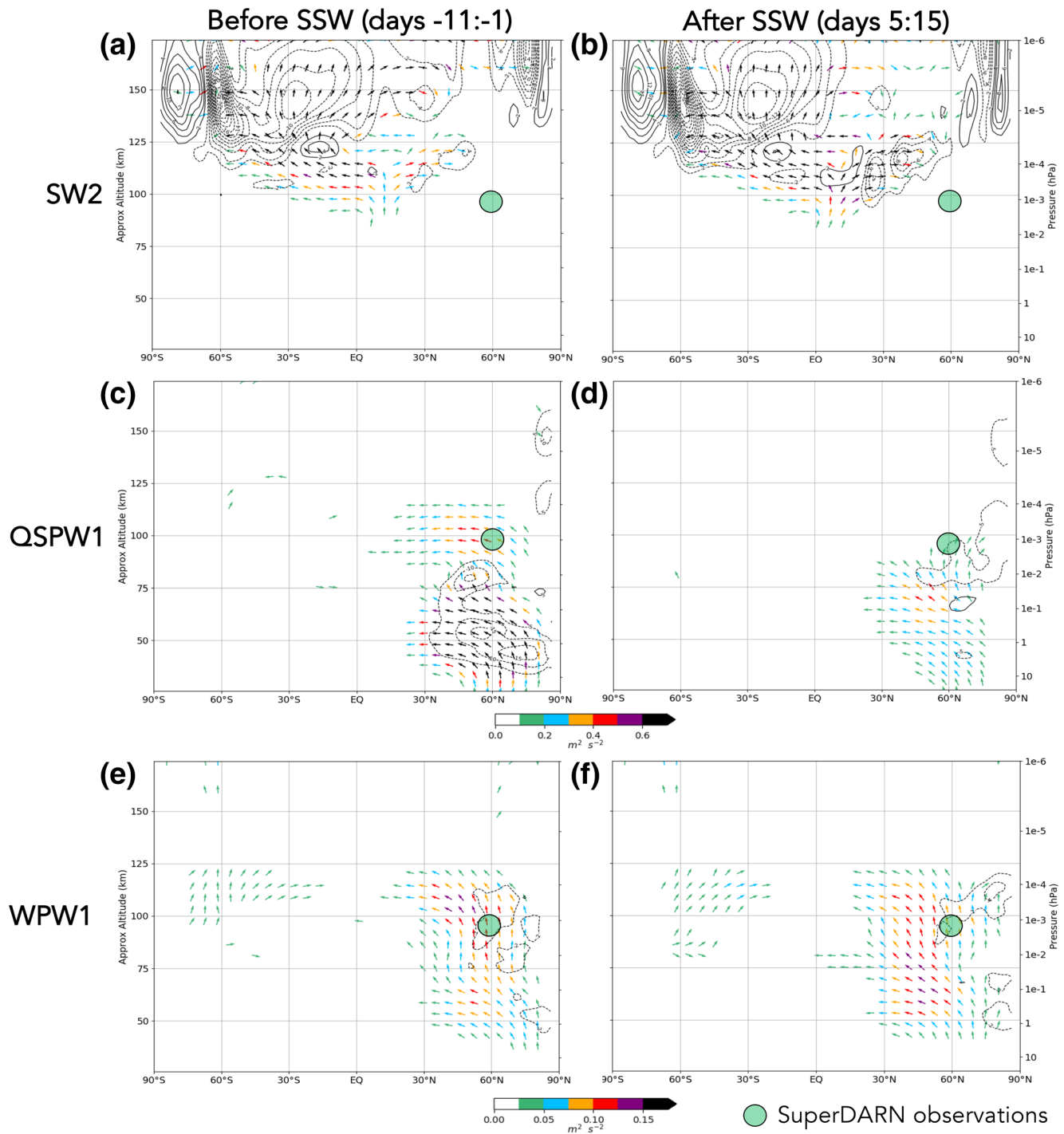
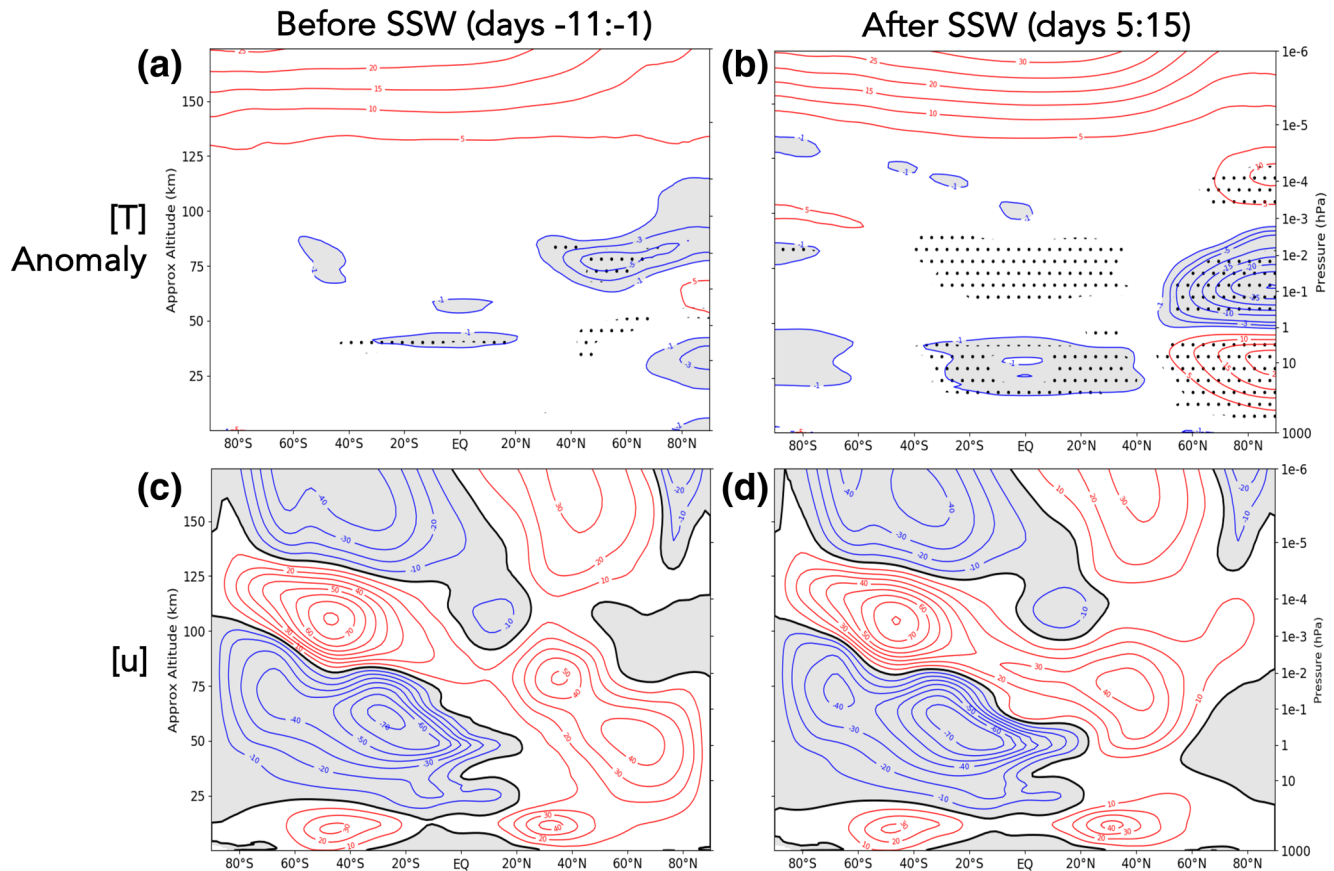


Figure 9. Same as Figure 8, except averaged between 115 and 125 km.

(e.g., Smith, 1997), SuperDARN observations (e.g., Stray et al., 2015a, 2015b), and model simulations (e.g., Smith, 2003), particularly in association with SSW (e.g., Limpasuvan et al., 2016). These waves may be associated with the longitudinally varying gravity wave drag due to the underlying planetary-scale wind variation (Smith, 2003).



**Figure 10.** Top row (a), (b) shows the altitude-latitude composite structure of the Eliassen-Palm (EP) flux (vectors) and its divergence (contours) during the 10-days averaged period before (left) and after (right) SSW onset. Solid contours show eastward acceleration and dashed westward acceleration, contoured every  $2 \text{ m s}^{-1} \text{ day}^{-1}$ . Middle row (c), (d) and bottom row (e), (f) shows the corresponding plots for QSPW1 and WPW1 with flux divergence contoured every 5 and  $2 \text{ m s}^{-1} \text{ day}^{-1}$ , respectively. All vectors are normalized and their colors show their magnitude. The green dot locates the approximate region of SuperDARN observations.



**Figure 11.** Top row (a), (b) shows the altitude-latitude composite structure of the zonal-mean temperature anomaly during the 10-days averaged period before (left) and after (right) SSW onset. Red contours show positive anomaly, contoured every 5 (K). Blue contours show negative anomaly, contoured every 2 (K). Stippling indicates where the  $t$ -test statistical significance level is above 95%. Bottom row (c), (d) shows the corresponding plots for the total zonal-mean zonal wind. Red contours show the eastward wind and blue the westward wind, contoured every  $10 \text{ m s}^{-1}$ . The westward wind is also shaded, and the zero wind line is in black.

Before SSW onset, the QSPW1 westward forcing is strong near the stratopause with a magnitude in excess of  $15 \text{ m s}^{-1} \text{ day}^{-1}$ . In response to QSPW1 driving, the (residual) mean meridional circulation after SSW onset intensifies with enhanced upwelling (and adiabatic cooling) over the equatorial region and increased downwelling (adiabatic heating) over the stratospheric winter pole. As confirmed in Figure 11b, the enhanced anomalous tropical cooling (gray regions) and polar warming (red contours) are evident in the zonal-mean temperature anomaly structure after SSW onset between 20 and 60 km. This simulated global temperature response captures the features reported in the observational study of the 2013 SSW by De Wit et al. (2015). We expect the significant tropical cooling to lead to a net increased production of equatorial stratospheric ozone (e.g., Limpasuvan et al., 2016). This consequently can result in an increase in solar heating that excites SW2, as suggested in Goncharenko et al. (2012). This excitation is consistent with the enhanced SW2 WAF illustrated in Figure 10b, and the positive SW2 amplitude anomaly in Figure 7d after SSW onset. Dedicated WACCM simulations of the 2009 SSW both with and without interactive ozone by Siddiqui et al. (2019) confirm the key role played by such an ozone increase in amplifying the tides by 10%–60%, albeit the temporal development of the tide in their simulations seemed to be set by the mean flow changes.

The polar stratospheric warming (indicated in Figure 11b) should weaken the eastward zonal-mean stratospheric polar jet (in Figure 11c), leading eventually to polar stratospheric wind reversal shown in Figure 11d in the Northern Hemisphere. The global zonal-mean zonal wind structure below 100 km consequently becomes more symmetric about the Equator, compared to the structure before SSW onset. As first noted by Jin et al. (2012), the reduction in the background wind asymmetry could give rise to the global response of SW2, as highlighted in Figure 7d. Theoretically, SW2 corresponds to the symmetric Hough mode (2,2)



(Forbes, 1995), which can become enhanced in the winter hemisphere as the background wind becomes more symmetric (Conte et al., 2019).

#### 4.3. Global Behaviors of SW1 and SW3 during SSWs

The top two rows of Figures 12 and 13 display the composite global SW1 and SW3 amplitude structures and their anomalies in response to SSW. Compared to SW2 (top two rows of Figure 7), these non-migrating semidiurnal tides are generally much weaker. Their total amplitudes tend to be larger in the Southern Hemisphere. Although our results here are for meridional wind, the overall dominance of SW3 over SW1 in the Northern Hemisphere is consistent with studies based on satellite tidal temperatures (Forbes et al., 2008; Pancheva & Mukhtarov, 2012). Before SSW, the SW1 and SW3 amplitude anomalies are positive in the Southern Hemisphere unlike SW2 anomalies (compare Figures 12c and 13c with Figure 7c). In the Northern Hemisphere, the amplitude anomalies are smaller, especially for SW3. After SSW, significant SW1 amplitude reduction occurs around 60°N and below 100 km, like SW2 in Figure 7d.

The latitude-time evolution of SW1 averaged between 91 and 97 km during SSW generally reveals stronger anomalies globally than SW3 (Figures 8e and 8f). The evolution of the anomalous SW1 and SW3 amplitudes is more robust and larger between 115 and 125 km (Figures 9e and 9f). At these higher levels, the amplitude enhancement of these non-migrating components occurs around SSW onset (day 0) near the equatorial region and at the middle to high Southern latitudes, just a few days before the SW2 growth in the Southern Hemisphere (Figure 9a). After day 5, the summer SW1 amplitude anomaly becomes negative. For the 2009 SSW event based on WACCM simulations with interactive ozone chemistry, Siddiqui et al. (2019) also noted that SW1 and SW3 can attain higher amplitudes in the summer mid-latitudes along with the strong development of SW2. In the Northern Hemisphere, the non-migrating semidiurnal tidal responses are more modest. Nonetheless, between 30°N and 70°N, the SW3 anomaly peaks around day 0, followed by the growth of SW1 around day 10. The illustrated middle to high latitude winter SW1 and SW3 amplification after SSW onset is consistent with the meridional cross-sections shown in Figures 12d and 13d.

Before SSW onset, the panels in the top two rows of Figures 10 indicate that QSPW1 activity can overlap with SW2. Correspondingly in Figures 8c and 9c, we see anomalously strong QSPW1 amplitudes in the middle to high winter altitudes prior to SSW onset (starting around day -20). The significant QSPW1 positive anomaly persists to around day 0 and is collocated, by then, with regions of strong SW2 positive anomaly seen in Figures 8a and 9a. The possible interaction between SW2 and QSPW1 during this spatiotemporal overlapping may qualitatively account for the bursts in SW1 and SW3 positive anomaly between 30°N and 60°N noted in Figures 8e, 8f, 9e, and 9f. Pedatella and Liu (2013) showed that the development of QSPWs was key in eliciting a SW1 response, maximizing in the summer hemisphere mid-latitudes, prior to SSW onset. However, the detailed timing of the SW2-QSPW1 interactions is not obvious and changes in the tidal waveguide may also play a role, as well as model biases, in explaining the discrepancies with observations. In their 2009 SSW case study, Pedatella et al. (2014) noted discrepancies among different models in the detailed day-to-day evolution of the SW1 response. The resultant response of SW1 and SW3 may also appear in other part of the globe (as suggested by Figures 12d and 13d).

We note that significant anomalous tidal response can occur leading up to SSW onset. Negative SW2 anomalies before SSW onset are evident mainly in the lower summer latitude band (e.g., Figures 7c and 9a). Such diminished SW2 response may be due to pre-existing background conditions that impact SW2 propagation and eventually facilitate SSW occurrence. The background winds are set up by drags exerted by gravity waves and various planetary waves such as those noted in Figures 10c, 10e for QSPW1 and WPW1. Furthermore, positive anomalies are evident in SW1 and SW3 before SSW onset in the summer hemisphere (e.g., Figures 9e, 9f, 12c, and 13c). The possible interaction between diminished SW2 and QSPW1 before SSW onset may account for the positive bursts of SW1 and SW3 in the summer hemisphere.

#### 4.4. Global Behaviors of $\tilde{S}W1$ and $\tilde{S}W3$ during SSWs

The interactions between SW2 and WPW1 may account for the presence of  $\tilde{S}W1$  and  $\tilde{S}W3$ . Figures 10e and 10f show WPW1 EP flux emanating from the winter middle stratosphere. Upon reaching the MLT, WPW1 WAF can overlap with SW2 (c.f., top row of Figure 10) even well after SSW onset. The latitude-time

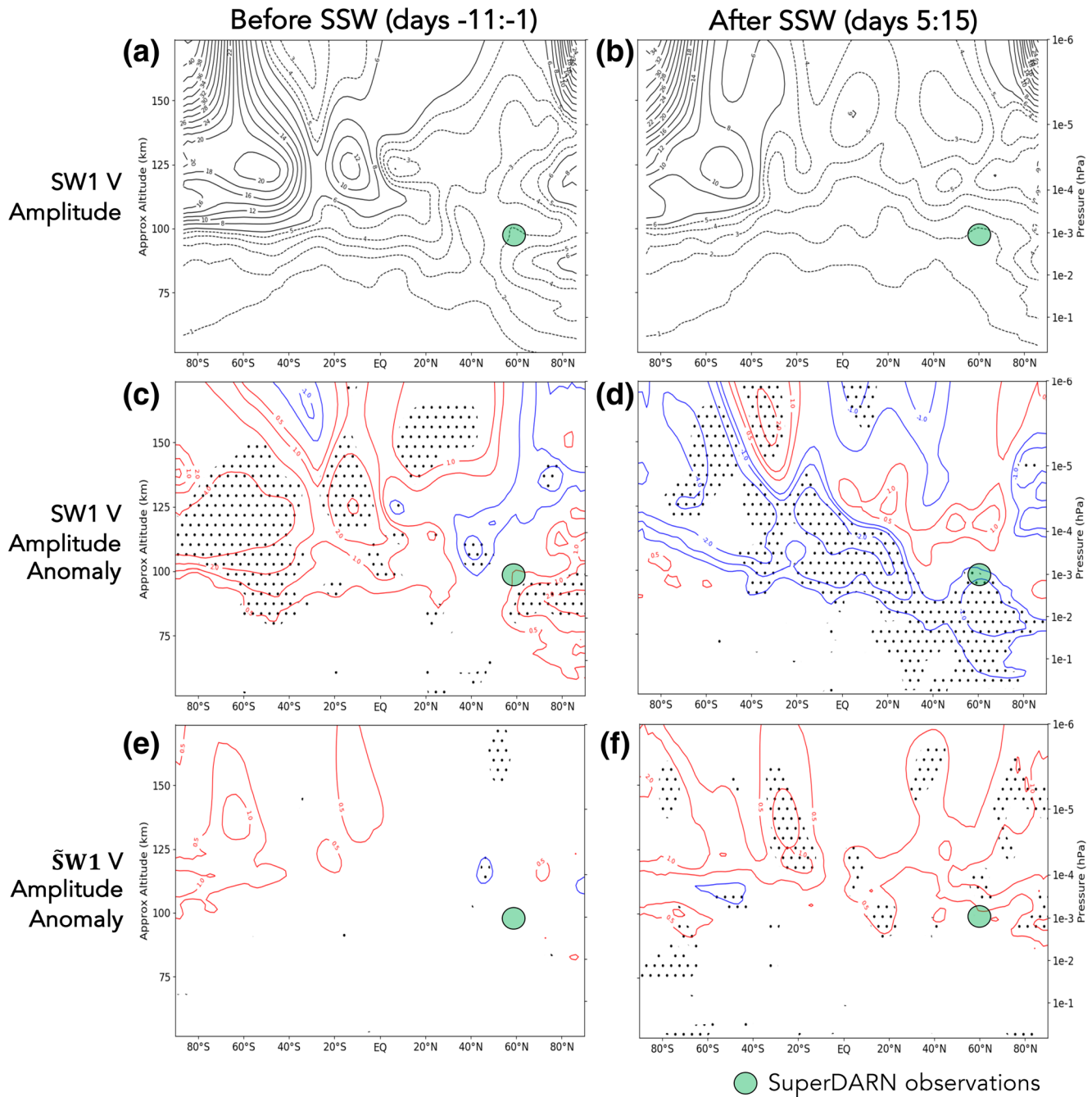


**Figure 12.** Top row (a), (b) shows the altitude-latitude composite structure of SW1 meridional wind amplitude during the 10-days averaged period before (left) and after (right) SSW onset. Solid contours are provided every  $2 \text{ m s}^{-1}$  and dashed contours every  $1 \text{ m s}^{-1}$  to accentuate smaller values. Middle row (c), (d) shows the corresponding plots for SW1 meridional wind amplitude anomaly. Bottom row (e), (f) shows the  $\tilde{S}W1$  meridional wind amplitude anomaly. The anomaly is defined as a departure from the climatological mean. Red contours show positive anomaly and blue the negative anomaly, contoured at 0.5, 1, 2, and  $4 \text{ m s}^{-1}$ . Stippling shows where the  $t$ -test statistical significance level is above 95%. The green dot locates the approximate region of the SuperDARN observations.

evolution of WPW1 amplitude anomalies in Figures 8d and 9d demonstrates that WPW1 becomes significantly positive poleward of  $30^\circ\text{N}$  around SSW onset and over a deep vertical layer. This enhancement slightly precedes the SW2 growth in the winter hemisphere (Figures 8a and 9a).

The  $\tilde{S}W1$  and  $\tilde{S}W3$  amplitude anomalies in the 10-days averaged meridional cross-sections are generally positive above 100 km (bottom rows of Figures 12 and 13). These anomalies become enhanced after SSW in the winter hemisphere. Although the amplitude anomalies are small (typically  $< 1 \text{ m s}^{-1}$  throughout the

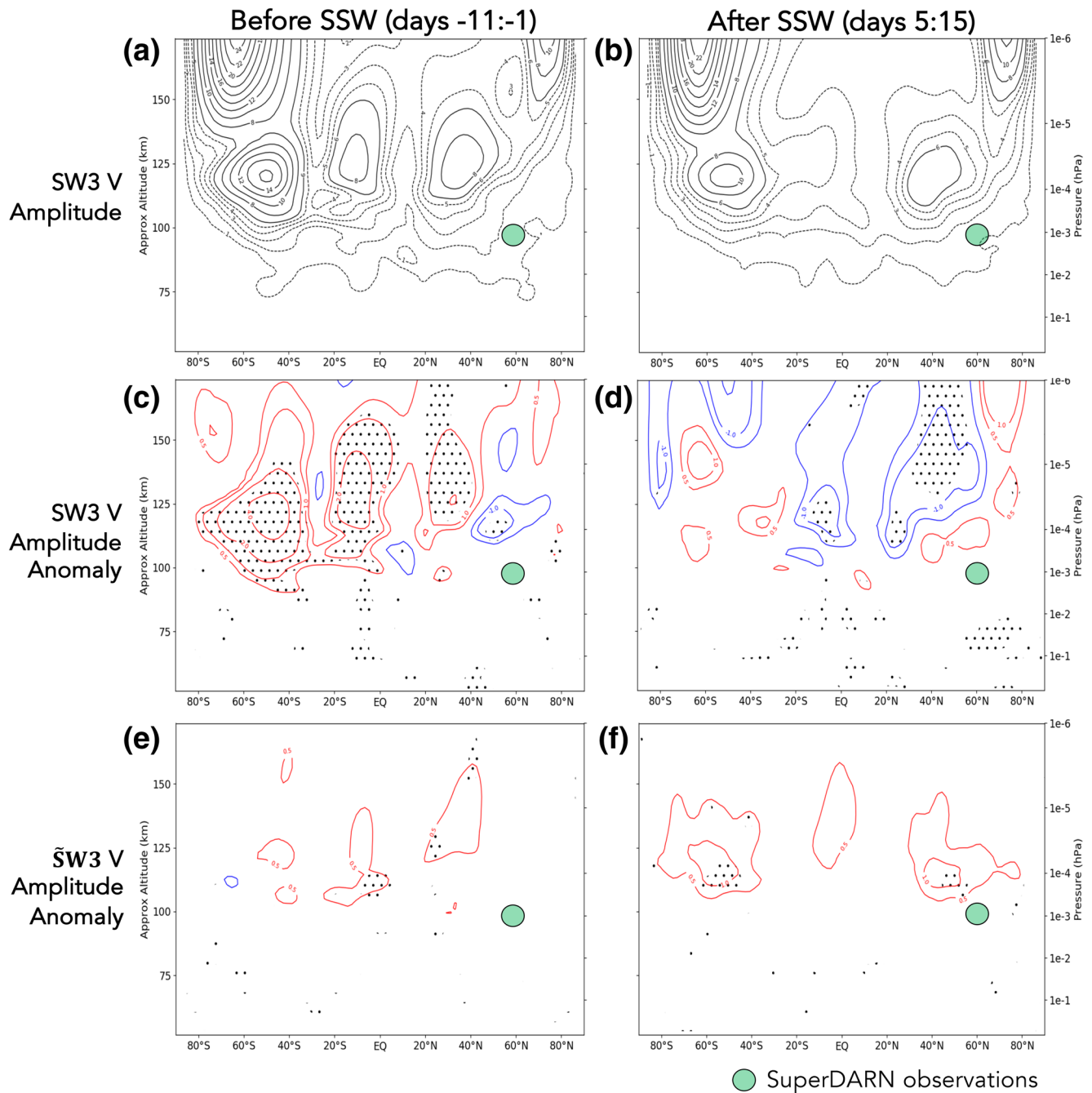


Figure 13. Same as Figure 12, except for SW3 and  $\tilde{S}W3$ .

MLT region), they are comparable to the modeled SW1 and SW3 anomalies. However, these small  $\tilde{S}W1$  and  $\tilde{S}W3$  enhancements may easily be attributed to SW1 and SW3 anomalies for short data series with inadequate spectral resolution to distinguish them, as suggested by He and Chau (2019).

#### 4.5. Global M2 Behaviors during SSWs

As mentioned in the Introduction, SSWs may elicit changes in M2, the migrating semidiurnal lunar tide. Dominant above 105 km, the M2 tide observed in SABER temperature tends to maximize in July and again in December between 10°N and 30°N (Forbes et al., 2013). In WACCM-X, the direct mechanism for M2

generation is absent without adding lunar tide forcing (e.g., Pedatella et al., 2012). Nonetheless, M2 signatures may still arise from the MERRA2 nudging below the stratopause, as done in SD-WACCM-X. To capture M2, we filter the SD-WACCM-X data for westward propagating signal between 12.29 and 12.63 h. Figure 5 shows the climatological M2 evolution (dashed black lines) averaged between 51°N and 66°N that also maximizes during similar months and becomes stronger with altitude (compare Figures 5c and 5d). Figure 7f illustrates a strong and significant global M2 enhancement in both hemispheres during SSWs. The composite M2 structure bears likeness to the WACCM-X results of Pedatella et al. (2012) but with weaker (stronger) amplitude in the winter (summer) hemisphere. Above 115 km, the dual-hemispheric positive M2 anomaly appears shortly after SSW onset and persists for over 20 days (Figure 9b). Although much smaller than SW2, the M2 response in the Northern Hemisphere exceeds that of SW1, SW3,  $\tilde{S}W1$ , and  $\tilde{S}W3$ .

#### 4.6. Eastward-Propagating Semidiurnal Tides during SSWs

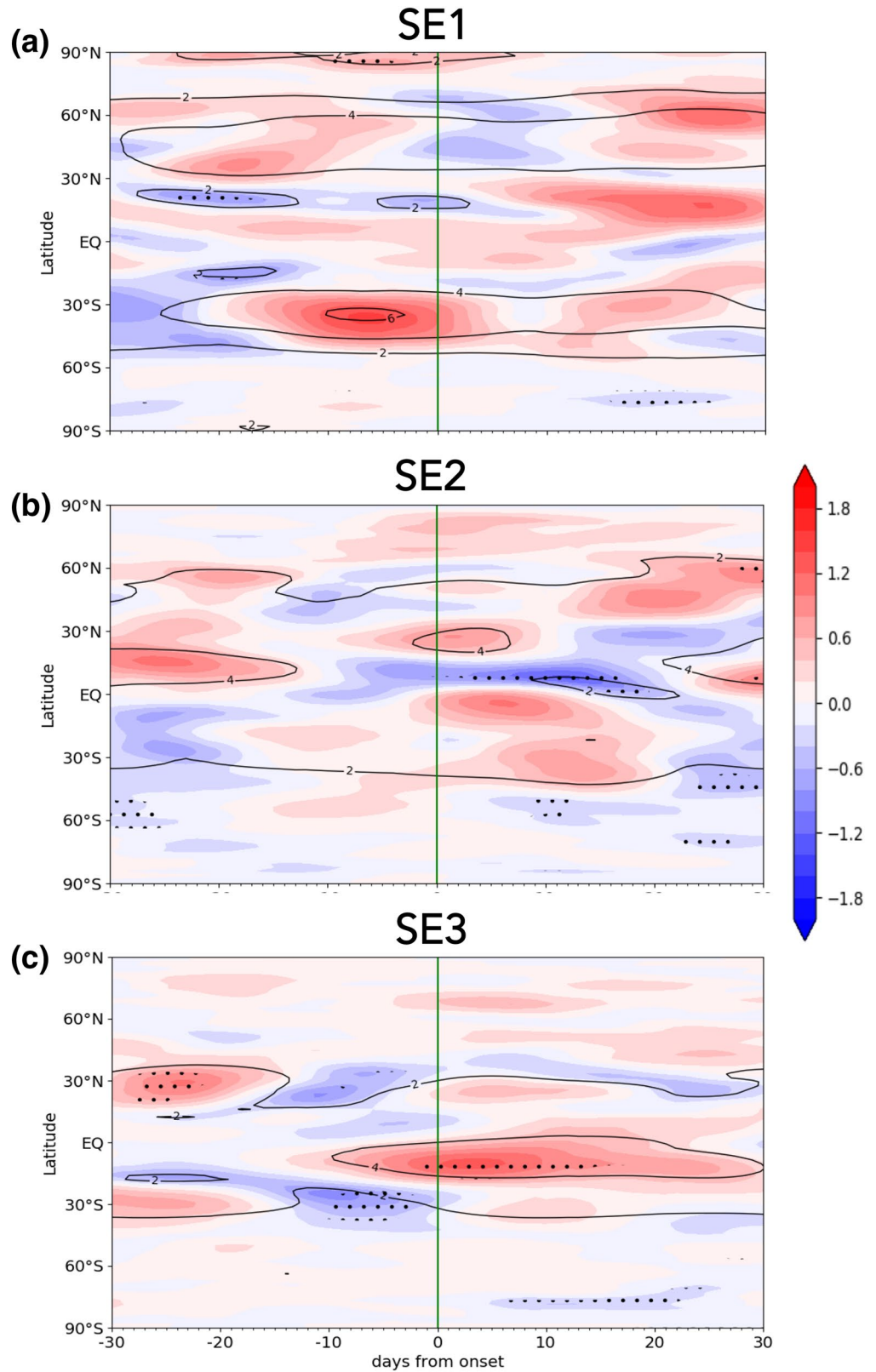
While not central to the thesis of this paper, we also examined the presence of eastward-propagating semidiurnal tides (i.e., SE) in the model to motivate future exploration. The SE climatology within the 40°N–40°S has been investigated using SABER data by Truskowski et al. (2014), who showed that they can occasionally attain similar amplitudes to the westward-propagating non-migrating tides, for example, in the Southern Hemisphere subtropics in summer. Depending of their wavenumbers, SEs can propagate upward from the underlying forcing regions but can also be generated in situ by non-linear interactions. In theory, the non-linear interactions between SE2 and QSPW1 may lead to the production of SE1 and SE3. However, they have not been discussed extensively in numerical simulations in the context of SSWs. An exception is Sassi et al. (2013) who showed the occurrences of SE1, SE2, and SE3 in temperature during January and February 2009 in a case study of the 2009 SSW using the previous version of WACCM-X. These authors found that the SE2 amplitude had a peak at northern mid-latitudes in that period.

Figure 14 shows the composite evolution of SE1, SE2, and SE3 for the 115–125 km altitude range. Analogous to the extraction of westward-propagating tides, the time series for zonal wavenumbers 1 and 3 were band-pass filtered to obtain eastward-propagating signatures with periods between 11.8 and 12.2 h to capture SEs. The SE anomalies are smaller than their westward-propagating counterparts in Figure 9. Significant negative SE2 response occurs after SSW onset in the 0°–30°N band and overlaps with significant negative QSPW1 seen in Figure 9c. The interactions between SE2 and QSPW1 may qualitatively account for the positive equatorial SE3 anomaly after SSW onset in Figure 14c.

## 5. Summary and Discussions

The aim of this study is to better understand the behaviors of westward-propagating semidiurnal tides in the MLT in response to SSWs. We first note the differences in the annual climatology of these tidal signatures between model and observations, which are probably due to discrepancies in the climatological background zonal wind in the altitude range of 80 and 100 km. The wind bias in the model can impact the amplitude and propagation of migrating tides and other slow-traveling PWs, and, thereby, the wave-wave interactions that may generate the non-migrating tidal components. Nevertheless, the broad characteristics of the SW2 climatology (except in winter) is well replicated in the model, with an amplitude that overwhelms SW1 and SW3 most of the year. During SSWs, the observed SW2 amplitude in the winter midlatitude declines just after the SSW onset and then enhances at 10 days later. The observed enhancement of SW1 and SW3 occurs at the same time. The corresponding simulated SW2 amplifies after SSW onset and peaks nearly the same time as the observations. The modeled SW1 and SW3 responses to SSWs are much weaker than observations. We acknowledge that we did not sample the model at observed locations to get a direct one-to-one comparison with SuperDARN.

The analyses of the long time series from the model allow us to use a higher spectral resolution to extract a smaller period range (albeit at the expense of the temporal resolution) for SW1, SW2, and SW3 to better isolate them from other semidiurnal-tide-like waves (i.e.,  $\tilde{S}W1$  and  $\tilde{S}W3$ ). While the climatology of the refined SW2 remains similar to observations, the SW2 response is more attenuated shortly after the SSW onset around the observed altitude range compared with using the broad filtering band (Figures 4d and



**Figure 14.** Latitude-time distribution of the composite meridional wind amplitude (line contours) and its anomaly (filled contours), averaged between 115 and 125 km, for (a) SE1, (b) SE2, and (c) SE3. The time is shown with respect to SSW onset (day 0, green line). Stippling indicates where the *t*-test statistical significance level is above 95%.

6c). However, a much stronger SW2 response to SSW in the model occurs above the observed altitude, with diminished amplitude before and enhancement after SSW onset in both hemispheres. The simulated SW2 enhancement likely arises from two influences, both induced by the circulation changes to SSW. The first influence is the increased tidal forcing due to the anomalous ozone heating in the stratosphere as a result of strong equatorial upwelling. The second is the decreased asymmetry of the background zonal-mean zonal wind as the winter polar vortex breaks down. In general, SW1 and SW3 tend to anomalously amplify just before SSW onset but mainly in the Southern Hemisphere. The model also suggests some overlap between SW2 and westward PWs of 10–20-day period that may result in  $\tilde{S}W1$  and  $\tilde{S}W3$  through non-linear interactions. These semidiurnal-tide-like waves amplify weakly (but on par with SW1 and SW3) after SSW onset in the Northern Hemisphere. As noted by He and Chau (2019), these semidiurnal-tide-like waves may contribute to observed changes in SW1 and SW3, if the analyzed data series is too short.

The generally favorable comparison between model and observations perhaps points to the improvement of this WACCM-X version, especially its new divergence damping scheme that reduces numerical damping on tides and its upgrades to improve tidal representation along with the relevant physics above the homopause. The simulated tides and the background circulation are still dependent on model parameters to address unresolved phenomena (e.g., diffusion, gravity waves). The model results may also be affected by persisting, unsolved model biases like the climatological background zonal wind in Figures 2 and 3. However, the background zonal wind biases in the model appear to be considerably less during SSW events. As suggested in Figure 11c, the predominantly westward zonal-mean zonal winds between 90 and 100 km at polar latitudes reverse to eastward in the two weeks following the onset. The daily peak value of  $25 \text{ m s}^{-1}$  (not shown) is in good agreement with the composite wind (based on 4 of the same SSW events) from specular meteor radar observations at Andenes (69,3°N) in Conte et al. (2019; see their Figure 2a).

While we did not process SuperDARN for eastward-propagating semidiurnal tides (i.e., SE), future investigations of eastward-propagating semidiurnal tides (SE) and their response to SSWs could be worthwhile as suggested by the model results. Furthermore, despite lacking the direct mechanism for M2 generation, SD-WACCM-X exhibit M2 response to SSWs potentially through nudging toward observations below the stratopause.

## Data Availability Statement

The CESM2.0 SD-WACCM-X hourly data was accessed through Earth System Grid (<https://www.earthsystemgrid.org>), called CESM run f. e20. FXSD.f19\_19.001 data. The Fitacf-level data containing the fitted backscatter returns for each beam and each range gate from each SuperDARN radar are available from <http://vt.superdarn.org>.

## Acknowledgments

JZ is supported by funding from the National Science Foundation (NSF) awards (RUI 1642232; REU 1560210). VL is supported by NSF Intergovernmental Panel Agreement. PJE and REH are supported in part by the Research Council of Norway/CoE under contract 223252/F50, and YOR by the project MADEIRA under Contract No. 274377. The authors acknowledge the computing and technical support from the NCAR Computation Information Systems Laboratory as well as the Coastal Carolina University cyberinfrastructure project (funded in part by NSF award MRI 1624068). The authors also appreciate suggestions provided by Hanli Liu at NCAR and the reviewers' comments that helped improve the initial draft of this paper.

## References

- Angelats i Coll, M., & Forbes, J. M. (2002). Nonlinear interactions in the upper atmosphere: The S = 1 and S = 3 nonmigrating semidiurnal tides. *Journal of Geophysical Research*, *107*(A8), 1157. <https://doi.org/10.1029/2001JA900179>
- Bhattacharya, Y., Shepherd, G. G., & Brown, S. (2004). Variability of atmospheric winds and waves in the Arctic polar mesosphere during a stratospheric sudden warming. *Geophysical Research Letters*, *31*(23). <https://doi.org/10.1029/2004GL020389>
- Chapman, S., & Lindzen, R. S. (1970). *Atmospheric tides* (pp. 201). Norwell, MA: D. Reidel.
- Chau, J. L., Hoffmann, P., Pedatella, N. M., Matthias, V., & Stober, G. (2015). Upper mesospheric lunar tides over middle and high latitudes during sudden stratospheric warming events. *Journal of Geophysical Research: Space Physics*, *120*, 3084–3096. <https://doi.org/10.1002/2015JA020998>
- Conte, J. F., Chau, J. L., & Peters, D. H. W. (2019). Middle- and high-latitude mesosphere and lower thermosphere mean winds and tides in response to strong polar-night jet oscillations. *Journal of Geophysical Research: Atmospheres*, *124*. <https://doi.org/10.1029/2019JD030828>
- Danabasoglu, G., Lamarque, J. F., Bacmeister, J., Bailey, D. A., DuVivier, A. K., Edwards, J., et al. (2020). The community earth system model version 2 (CESM2). *Journal of Advances in Modeling Earth Systems*, *12*(2), e2019MS001916. <https://doi.org/10.1029/2019MS001916>
- De Wit, R. J., Hibbins, R. E., Espy, P. J., & Hennem, E. A. (2015). Coupling in the middle atmosphere related to the 2013 major Sudden Stratospheric Warming. *Annals of Geophysics*, *33*(3), 309–319. <https://doi.org/10.5194/angeo-33-309-2015>
- De Wit, R. J., Hibbins, R. E., Espy, P. J., Orsolini, Y. J., Limpasuvan, V., & Kinnison, D. (2014). Observations of gravity wave forcing of the mesopause region during the January 2013 major Sudden Stratospheric Warming. *Geophysical Research Letters*, *41*. <https://doi.org/10.1002/2014GL060501>
- Espy, P. J., Stegman, J., & Witt, G. (1997). Interannual variations of the quasi-16-day oscillation in the polar summer mesospheric temperature. *Journal of Geophysical Research*, *102*(D2), 1983–1990. <https://doi.org/10.1029/96JD02717>
- Farley, D. T. (1972). Multi-pulse incoherent scatter correlation function measurements. *Radio Science*, *7*, 661–666.
- Forbes, J. M. (1984). Middle atmosphere tides. *Journal of Atmospheric and Terrestrial Physics*, *46*(11), 1049–1067.

- Forbes, J. M. (1995). Tidal and planetary waves. In R. M. Johnson, & T. L. Killeen (Eds.), *The upper mesosphere and lower thermosphere: A Review of experiment and theory, geophysical monograph series*. Vol. 87.
- Forbes, J. M., Hagan, M. E., Zhang, X., & Hamilton, K. (1997). Upper atmosphere tidal oscillations due to latent heat release in the tropical troposphere. *Annales geophysicae*, Vol. 15 (pp. 1165–1175). Springer-Verlag. <https://doi.org/10.1007/s00585-997-1165-0>
- Forbes, J. M., & Zhang, X. (2012). Lunar tide amplification during the January 2009 stratosphere warming event: Observations and theory. *Journal of Geophysical Research*, *117*(A12). <https://doi.org/10.1029/2012JA017963>
- Forbes, J. M., Zhang, X., Bruinsma, S., & Oberheide, J. (2013). Lunar semidiurnal tide in the thermosphere under solar minimum conditions. *Journal of Geophysical Research: Space Physics*, *118*(4), 1788–1801. <https://doi.org/10.1029/2012JA017962>
- Forbes, J. M., Zhang, X., Palo, S., Russell, J., Mertens, C. J., & Mlynczak, M. (2008). Tidal variability in the ionospheric dynamo region. *Journal of Geophysical Research*, *113*(A2). <https://doi.org/10.1029/2007JA012737>
- Forbes, J. M., Zhang, X., Talaat, E. R., & Ward, W. (2003). Nonmigrating diurnal tides in the thermosphere. *Journal of Geophysical Research*, *108*, 1033. <https://doi.org/10.1029/2002JA009262>
- García, R. R., Smith, A. K., Kinnison, D. E., de la Camara, A., & Murphy, D. J. (2017). Modification of the gravity wave parameterization in the Whole Atmosphere Community Climate Model: Motivation and results. *Journal of the Atmospheric Sciences*, *74*, 275–291. <https://doi.org/10.1175/JAS-D-16-0104.1>
- Gelaro, R., McCarty, W., Suárez, M. J., Todling, R., Molod, A., Takacs, L., et al. (2017). The modern-era retrospective analysis for research and applications, version 2 (MERRA-2). *Journal of Climate*, *30*(14), 5419–5454. <https://doi.org/10.1175/JCLI-D-16-0758.1>
- Goncharenko, L. P., Coster, A. J., Plumb, R. A., & Domeisen, D. I. V. (2012). The potential role of stratospheric ozone in the stratosphere-ionosphere coupling during stratospheric warmings. *Geophysical Research Letters*, *39*, L08101. <https://doi.org/10.1029/2012GL051261>
- Hagan, M. E., & Forbes, J. M. (2003). Migrating and nonmigrating semidiurnal tides in the upper atmosphere excited by tropospheric latent heat release. *Journal of Geophysical Research*, *108*(A2), 1062. <https://doi.org/10.1029/2002JA009466>
- Hall, G. E., MacDougall, J. W., Moorcroft, D. R., St-Maurice, J.-P., Manson, A. H., & Meek, C. E. (1997). Super Dual Auroral Radar Network observations of meteor echoes. *Journal of Geophysical Research*, *102*, 14603–14614. <https://doi.org/10.1029/97JA00517>
- He, M., & Chau, J. L. (2019). Mesospheric semidiurnal tides and near-12 h waves through jointly analyzing observations of five specular meteor radars from three longitudinal sectors at boreal midlatitudes. *Atmospheric Chemistry and Physics*, *19*(9), 5993–6006. <https://doi.org/10.5194/acp-19-5993-2019>
- He, M., Chau, J. L., Stober, G., Hall, C. M., Tsutsumi, M., & Hoffmann, P. (2017). Application of Manley-Rowe relation in analyzing non-linear interactions between planetary waves and the solar semidiurnal tide during 2009 sudden stratospheric warming event. *Journal of Geophysical Research: Space Physics*, *122*, 10783–10795. <https://doi.org/10.1002/2017JA024630>
- Hibbins, R. E., Espy, P. J., Orsolini, Y. J., Limpasuvan, V., & Barnes, R. J. (2019). SuperDARN observations of semidiurnal tidal variability in the MLT and the response to sudden stratospheric warming events. *Journal of Geophysical Research Atmospheres*, *124*, 4862–4872. <https://doi.org/10.1029/2018JD030157>
- Hibbins, R. E., Jarvis, M. J., & Ford, E. A. K. (2009). Quasi-biennial oscillation influence on long-period planetary waves in the Antarctic upper mesosphere. *Journal of Geophysical Research*, *114*. <https://doi.org/10.1029/2008JD011174>
- Hocking, W. K., Fuller, B., & Vandepeter, B. (2001). Real-time determination of meteor-related parameters utilizing modem digital technology. *Journal of Atmospheric and Solar-Terrestrial Physics*, *63*(2–3), 155–169. [http://dx.doi.org/10.1016/S1364-6826\(00\)00138-3](http://dx.doi.org/10.1016/S1364-6826(00)00138-3)
- Imura, H., Fritts, D. C., Wu, Q., Skinner, W. R., & Palo, S. E. (2010). Nonmigrating semidiurnal tide over the Arctic determined from TIMED Doppler Interferometer wind observations. *Journal of Geophysical Research*, *115*, D06109. <https://doi.org/10.1029/2009JD012733>
- Jin, H., Miyoshi, Y., Pancheva, D., Mukhtarov, P., Fujiwara, H., & Shinagawa, H. (2012). Response of migrating tides to the stratospheric sudden warming in 2009 and their effects on the ionosphere studied by a whole atmosphere ionosphere model GAIA with COSMIC and TIMED/SABER observations. *Journal of Geophysical Research*, *117*, A10323. <https://doi.org/10.1029/2012JA017650>
- Kleinknecht, N. H., Espy, P. J., & Hibbins, R. E. (2014). The climatology of zonal wave numbers 1 and 2 planetary wave structure in the MLT using a chain of Northern Hemisphere SuperDARN radars. *Journal of Geophysical Research: Atmospheres*, *119*(3), 1292–1307. <https://doi.org/10.1002/2013JD019850>
- Limpasuvan, V., Orsolini, Y. J., Chandran, A., Garcia, R. R., & Smith, A. K. (2016). On the composite response of the MLT to major sudden stratospheric warming events with elevated stratopause. *Journal of Geophysical Research Atmospheres*, *121*, 4518–4537. <https://doi.org/10.1002/2015JD024401>
- Lin, J. T., Lin, C. H., Lin, C. Y., Pedatella, N. M., Rajesh, P. K., Matsuo, T., et al. (2019). Revisiting the modulations of ionospheric solar and lunar migrating tides during the 2009 stratospheric sudden warming by using global ionosphere specification. *Space Weather*, *17*(5), 767–777. <https://doi.org/10.1029/2019SW002184>
- Liu, H.-L., & co-authors (2018). Development and validation of the Whole Atmosphere Community Climate Model with thermosphere and ionosphere extension (WACCM-X). *Journal of Advances in Modeling Earth Systems*, *10*. <https://doi.org/10.1002/2017MS001232>
- Liu, H.-L., Wang, W., Richmond, A. D., & Roble, R. G. (2010). Ionospheric variability due to planetary waves and tides for solar minimum conditions. *Journal of Geophysical Research: Space Physics*, *115*, A00G01. <https://doi.org/10.1029/2009JA015188>
- Marsh, D. R., Mills, M. J., Kinnison, D. E., Lamarque, J.-F., Calvo, N., & Polvani, L. M. (2013). Climate change from 1850 to 2005 simulated in CESM1(WACCM). *Journal of Climate*, *26*, 7372–7391. <https://doi.org/10.1175/JCLI-D-12-00558.1>
- McDonald, A. J., Hibbins, R. E., & Jarvis, M. J. (2011). Properties of the quasi 16 day wave derived from EOS MLS observations. *Journal of Geophysical Research: Atmosphere*, *116*. <https://doi.org/10.1029/2010JD014719>
- Miyoshi, Y., Pancheva, D., Mukhtarov, P., Jin, H., Fujiwara, H., & Shinagawa, H. (2017). Excitation mechanism of non-migrating tides. *Journal of Atmospheric and Solar-Terrestrial Physics*, *156*, 24–36. <https://doi.org/10.1016/j.jastp.2017.02.012>
- Nozawa, S., Hall, C. M., Tsutsumi, M., Brekke, A., Ogawa, Y., Tsuda, T. T., et al. (2012). Mean winds, tides, and quasi-2 day waves above Bear Island. *Journal of Atmospheric and Solar-Terrestrial Physics*, *90*, 26–44. <https://doi.org/10.1016/j.jastp.2012.05.002>
- Orsolini, Y. J., Limpasuvan, V., Pérot, K., Espy, P. J., Hibbins, R., Lossow, S., et al. (2017). Modelling the descent of NO during the Elevated Stratopause Event of January 2013. *Journal of Atmospheric and Solar-Terrestrial Physics*, *155*, 50–61. <https://doi.org/10.1016/j.jastp.2017.01.006>
- Pancheva, D., & Mukhtarov, P. (2012). Global Response of the Ionosphere to Atmospheric Tides Forced from Below: Recent Progress Based on Satellite Measurements. *Space Science Reviews*, *168*, 175–209. <https://doi.org/10.1007/s11214-011-9837-1>
- Pediatella, N. M., et al. (2014). The neutral dynamics during the 2009 sudden stratosphere warming simulated by different whole atmosphere models. *Journal of Geophysical Research: Space Physics*, *119*, 1306–1324. <https://doi.org/10.1002/2013JA019421>
- Pediatella, N. M., Fang, T. W., Jin, H., Sassi, F., Schmidt, H., Chau, J. L., et al. (2016). Multimodel comparison of the ionosphere variability during the 2009 sudden stratosphere warming. *Journal of Geophysical Research: Space Physics*, *121*(7), 7204–7225. <https://doi.org/10.1002/2016JA022859>

- Pedatella, N. M., & Forbes, J. M. (2010). Evidence for stratosphere sudden warming-ionosphere coupling due to vertically propagating tides. *Geophysical Research Letters*, *37*, L11104. <https://doi.org/10.1029/2010GL043560>
- Pedatella, N. M., & Liu, H. L. (2013). The influence of atmospheric tide and planetary wave variability during sudden stratosphere warmings on the low latitude ionosphere. *Journal of Geophysical Research: Space Physics*, *118*(8), 5333–5347. <https://doi.org/10.1002/jgra.50492>
- Pedatella, N. M., Liu, H.-L., Richmond, A. D., Maute, A., & Fang, T.-W. (2012). Simulations of solar and lunar tidal variability in the mesosphere and lower thermosphere during sudden stratosphere warmings and their influence on the low-latitude ionosphere. *Journal of Geophysical Research*, *117*. <https://doi.org/10.1029/2012JA017858>
- Qian, L. Y., Burns, A. G., Emery, B. A., Foster, B., Lu, G., Maute, A., et al. (2014). The NCAR TIE-GCM: A community model of the coupled thermosphere/ionosphere system. In J. Huba, R. Schunk, & G. Khazanov (Eds.), *Modeling the ionosphere and thermosphere system, Geophysical monograph series* (pp. 73). Chichester, UK: John Wiley. <https://doi.org/10.1002/9781118704417.ch7>
- Richter, J. H., Sassi, F., & Garcia, R. R. (2010). Toward a physically based gravity wave source parameterization in a general circulation model. *Journal of the Atmospheric Sciences*, *67*, 136–156. <https://doi.org/10.1175/2009JAS3112.1>
- Salby, M. L. (1982). Sampling theory for synoptic satellite observations, part II: fast Fourier synoptic mapping. *Journal of the Atmospheric Sciences*, *39*, 2577–2600.
- Sassi, F., Liu, H.-L., Ma, J., & Garcia, R. R. (2013). The lower thermosphere during the northern hemisphere winter of 2009: A modeling study using high-altitude data assimilation products in WACCM-X. *Journal of Geophysical Research: Atmospheres*, *118*, 8954–8968. <https://doi.org/10.1002/jgrd.50632>
- Siddiqui, T. A., Maute, A., & Pedatella, N. M. (2019). On the importance of interactive ozone chemistry in Earth-System models for studying mesosphere-lower thermosphere tidal changes during sudden stratospheric warmings. *Journal of Geophysical Research: Space Physics*, *124*. <https://doi.org/10.1029/2019JA027193>
- Smith, A. (1997). Stationary Planetary Waves in Upper Mesospheric Winds. *Journal of the Atmospheric Sciences*, *54*, 2. [https://doi.org/10.1175/1520-0469\(1997\)054<2129:SPWIUM>2.0.CO](https://doi.org/10.1175/1520-0469(1997)054<2129:SPWIUM>2.0.CO)
- Smith, A. (2003). The origin of stationary planetary waves in the upper mesosphere. *Journal of the Atmospheric Sciences*, *60*, 2. [https://doi.org/10.1175/1520-0469\(2003\)060<3033:TOOSPW>2.0.CO](https://doi.org/10.1175/1520-0469(2003)060<3033:TOOSPW>2.0.CO)
- Sridharan, S. (2019). Seasonal variations of low-latitude migrating and nonmigrating diurnal and semidiurnal tides in TIMED-SABER temperature and their relationship with source variations. *Journal of Geophysical Research: Space Physics*, *124*(5), 3558–3572. <https://doi.org/10.1029/2018JA026190>
- Stray, N. H., Espy, P. J., Limpasuvan, V., & Hibbins, R. E. (2015b). Characterization of Quasi-Stationary Planetary Wave in the Northern MLT during Summer. *Journal of Atmospheric and Solar-Terrestrial Physics*. <https://doi.org/10.1016/j.jastp.2014.12.003>
- Stray, N., Orsolini, Y., Espy, P., Limpasuvan, V., & Hibbins, R. R. (2015a). Observations of PW activity in the MLT during SSW events using a chain of SuperDARN radars and SD-WACCM. *Atmospheric Chemistry and Physics Discussions*, *15*(1), 393–413.
- Teitelbaum, H., & Vial, F. (1991). On tidal variability by nonlinear interaction with planetary waves. *Journal of Geophysical Research*, *96*(A8), 14169–14214. <https://doi.org/10.1029/91JA01019>
- Truskowski, A., Forbes, J., Zhang, X., & Palo, S. (2014). New perspectives on the thermosphere tides: 1. Lower thermosphere spectra and seasonal-latitude structure. *Earth Planets and Space*, *66*, 136. <https://doi.org/10.1186/s40623-014-0136-4>
- Wang, H., Fuller-Rowell, T. J., Akmaev, R. A., Hu, M., Kleist, D. T., & Iredell, M. D. (2011). First simulations with a whole atmosphere data assimilation and forecast system: The January 2009 major sudden stratospheric warming. *Journal of Geophysical Research*, *116*(A12). <https://doi.org/10.1029/2011JA017081>
- Wu, D. L., Hays, P. B., & Skinner, W. R. (1995). A least squares method for spectral analysis of space-time series. *Journal of the Atmospheric Sciences*, *52*(20), 3501–3511. [https://doi.org/10.1175/1520-0469\(1995\)052<3501:ALSMFS>2.0.CO;2](https://doi.org/10.1175/1520-0469(1995)052<3501:ALSMFS>2.0.CO;2)